

Monitoring Aerosol - Cloud Interactions in Liquid Water Clouds

Sarna, K.

DOI

[10.4233/uuid:42c5bef9-8195-42a5-a103-49b8bbbc2d96](https://doi.org/10.4233/uuid:42c5bef9-8195-42a5-a103-49b8bbbc2d96)

Publication date

2021

Document Version

Final published version

Citation (APA)

Sarna, K. (2021). *Monitoring Aerosol - Cloud Interactions in Liquid Water Clouds*. [Dissertation (TU Delft), Delft University of Technology]. <https://doi.org/10.4233/uuid:42c5bef9-8195-42a5-a103-49b8bbbc2d96>

Important note

To cite this publication, please use the final published version (if applicable).
Please check the document version above.

Copyright

Other than for strictly personal use, it is not permitted to download, forward or distribute the text or part of it, without the consent of the author(s) and/or copyright holder(s), unless the work is under an open content license such as Creative Commons.

Takedown policy

Please contact us and provide details if you believe this document breaches copyrights.
We will remove access to the work immediately and investigate your claim.

Monitoring Aerosol–Cloud Interactions

in Liquid Water Clouds

Monitoring Aerosol–Cloud Interactions

in Liquid Water Clouds

Proefschrift

ter verkrijging van de graad van doctor
aan de Technische Universiteit Delft,
op gezag van de Rector Magnificus Prof.dr.ir. T.H.J.J. van der Hagen voorzitter van
het College voor Promoties,
in het openbaar te verdedigen op donderdag 21 januari 2021 om 12:30 uur

door

Karolina SARNA

Master of Science in Environmental Protection
Technische Universiteit Warschau, Polen
geboren te Warschau, Polen.

Dit proefschrift is goedgekeurd door de promotor: Prof. dr. ir. H.W.J. Russchenberg

Samenstelling promotiecommissie:

Rector Magnificus, voorzitter
Prof. dr. ir. H.W.J. Russchenberg, Technische Universiteit Delft, promotor

Onafhankelijke leden:

Prof. dr. P.F. Levelt, Technische Universiteit Delft
Prof. dr. U. Löhnert, The University of Cologne
Prof. dr. E. O'Connor, Finnish Meteorological Institute
Dr. G. Biskos, The Cyprus Institute
Dr. F. Glassmeier, Technische Universiteit Delft
Prof. dr. A.P. Siebesma, Technische Universiteit Delft, reservelid

Other members:

Dr. D.P. Donovan, Koninklijk Nederlands Meteorologisch Instituut

Dr. D.P. Donovan heeft als begeleider in belangrijke mate aan de totstandkoming van het proefschrift bijgedragen.



The research leading to these results was part of the ACTRIS project that received funding from the European Union Seventh Framework Programme (FP7/2007-2013) under grant agreement 262254.

Keywords: aerosol, clouds, aerosol-clouds interactions, remote sensing

Printed by: Printer Pro

Copyright © 2021 by K. Sarna

ISBN 000-00-0000-000-0

An electronic version of this dissertation is available at

<http://repository.tudelft.nl/>.

*You'll never know everything about anything,
especially something you love.*

Julia Child

Contents

Summary	1
Samenvatting	3
1 Introduction	5
1.1 Motivation	5
1.2 Aerosol - cloud interactions	5
1.2.1 What are aerosols?	5
1.2.2 Influence of aerosols on climate	6
1.2.3 Understanding aerosols - cloud interactions	7
1.3 This thesis	8
References	9
2 Scheme for monitoring aerosol-cloud interactions	11
2.1 Introduction	13
2.2 Quantifying interactions between aerosols and cloud	14
2.2.1 Aerosols and Cloud Properties Proxies	16
2.2.2 Relation between Aerosols and Cloud Proxies	17
2.3 Methodology	17
2.3.1 Instrumentation and Data set	17
2.3.2 Data Selection Criteria	19
2.4 Application of the method to observations from Graciosa Is- land, Azores	20
2.4.1 Study case from 3 November 2009	21
2.4.2 Study case from 29 November 2009	24
2.4.3 Comparison of example study cases	26
2.5 Summary and Outlook	31
References	33
3 Aerosol-Cloud Interactions at CESAR Observatory	37
3.1 Introduction	39
3.2 Theoretical basis of aerosol-cloud interactions	40
3.3 Methodology of an ACI monitoring scheme	41
3.3.1 Data selection criteria	42
3.4 Observations from CESAR Observatory	42
3.4.1 Instrumentation	43
3.4.2 Aerosols background at CESAR	44
3.4.3 Selected dataset	44

3.5	Results and discussion	44
3.5.1	ACI metrics	44
3.5.2	Impact of updrafts	49
3.5.3	Relation with <i>LWP</i>	49
3.5.4	Relation between correlation coefficient (<i>r</i>) and ACI_r	51
3.6	Summary and conclusions	52
	References	56
4	Optical extinction of liquid water clouds	59
4.1	Introduction	61
4.2	Lidar signal inversion	61
4.3	ECSIM Simulations	62
4.4	Inversion results	63
4.4.1	Difficulties in inversion steps	63
4.4.2	Estimating cloud base height	69
4.4.3	Signal inversion error and accuracy	71
4.4.4	Impact of α_0 estimation	72
4.5	Conclusions	75
4.6	Appendix A - Derivation of the resolution correction	77
	References	80
5	Summary and Outlook	83
5.1	Summary	84
5.2	Outlook	85
	References	86
	Curriculum Vitæ	87
	List of Publications	89
	Acknowledgments	90

Summary

This thesis presents a new method for the continuous observation of aerosol-cloud interactions with ground-based remote sensing instruments. The described method is based on the measurements from UV lidar, radar and radiometer. All of those instruments are capable of obtaining continuous, high-resolution measurements. In order to facilitate its easy implementation to measuring sites the method is based on a standardized Cloudnet data format. The main goal is to monitor the change in the cloud droplet concentration, as obtained from the measurements by cloud radar and radiometer, to then compare it to the aerosol background below the cloud, represented by the attenuated backscatter measured by UV lidar. The response of the cloud to the aerosol background can best be measured when the amount of available water is kept constant. Hence the measurements from the radiometer, specifically the derived liquid water path (LWP), which is used to constrain the cloud response. Based on the value of the LWP, analyzed data is divided into bins and for each of these the relation between cloud droplet effective radius and integrated value of the attenuated backscatter are calculated. This metric is called ACI_r and is used to describe the strength of the relation between the clouds microphysical properties and the aerosol background below the cloud. The method was first tested and applied to pristine marine clouds as measured at the Graciosa Island in the Azores. The application was then extended to the Cabauw site located in the Netherlands. On both sites a decrease in the cloud size was observed in combination with a simultaneous increase of the aerosol loading below the cloud. This relation was particularly strong for a mid range of the LWP, between 40 and 60 gm^{-2} LWP for the cases from Azores and between 60 and 105 gm^{-2} for the cases from the Netherlands. These results indicate that the process of aerosol-cloud interactions is a predominant one only under those conditions where a mid amount of water is available. When the amount of available water is less than 40 gm^{-2} this process is harder to observe, due to the initial stage of cloud formation. In the case of LWP above 105 gm^{-2} other cloud processes, such as collision and coalescence, seem to be predominant. The results from the analysis of the Cabauw dataset, which was the more extensive dataset, also made clear that updraft within the cloud plays a significant role in invigorating aerosol particles into becoming cloud droplets. A possible extension of the presented method includes obtaining optical cloud extinction from the UV lidar measurements. The presented retrieval method can obtain very reliable results when compared to the simulated results. Hence the cloud optical extinction can be used as a proxy of the cloud properties and the described method of monitoring aerosol-cloud interactions can be applied to measurement sites where only UV lidar and radiometer are present. This thesis shows that ground-based remote sensing instruments used in synergy can efficiently and continuously monitor aerosol-cloud interactions.

Samenvatting

Dit proefschrift stelt een nieuwe methodiek voor die bestaat uit de continue monitoring van aerosol-wolk interacties door teledetectie vanaf de grond. De methode is gebaseerd op de metingen van UV-lidar, radar en een radiometer. Deze instrumenten kunnen voortdurend en met een hoge resolutie metingen doen. Om een implementatie van de methode eenvoudig in te kunnen voeren op de meetlocaties is de methode gebaseerd op een gestandaardiseerd Cloudnet dataformaat. Het primaire doel van de methode is om de verandering in de concentratie van de wolkeendruppels, zoals verkregen uit de metingen met een wolken-radar en de radiometer, te volgen en deze te vergelijken met de aerosol-background onder de wolk, verkregen door middel van de attenuated backscatter zoals gemeten door UV-lidar. De reactie van de wolk op de aerosol-background kan het beste worden gemeten wanneer de hoeveelheid beschikbaar water constant is. Hiertoe worden de metingen van de radiometer, met name van het liquid water path (LWP), gebruikt om de wolkrespons vast te zetten. Op basis van de waarde van het geanalyseerde LWP worden de gegevens verdeeld in data-bereiken. Voor elk bereik wordt de relatie tussen de effectieve straal van de wolkeendruppel en de geïntegreerde waarde van de attenuated backscatter berekend. Deze statistiek wordt ACI_r genoemd en wordt gebruikt om de sterkte van de relatie tussen de microfysische eigenschappen van de wolk en de aerosol-background onder de wolk te definiëren. De methodiek is voor het eerst getest en toegepast op ongerepte zeewolken, zoals gemeten op het Graciosa-eiland, onderdeel van de Azoren. De methodiek is hierna verder toegepast op de Cabauw-site in Nederland. Op beide sites werd een afname van de wolk grootte waargenomen met een gelijktijdige toename van de aerosolbelasting onder de wolk. Deze relatie was bijzonder sterk voor een middenbereik van de LWP, te weten tussen 40 en 60 $g \cdot m^{-2}$ LWP voor de metingen uit de Azoren en tussen 60 en 105 $g \cdot m^{-2}$ voor de resultaten in Nederland. Deze resultaten geven aan dat het proces van aerosol-wolkinteracties alleen de overhand heeft in die omstandigheden waarin een gemiddelde hoeveelheid water beschikbaar is. Wanneer de hoeveelheid beschikbaar water minder is dan 40 $g \cdot m^{-2}$, is dit proces lastiger te observeren vanwege de beginfase van wolkenvorming. Wanneer het LWP 105 $g \cdot m^{-2}$ overstijgt, lijken andere processen binnen de wolk, zoals botsing en coalescentie, overheersend te zijn. Uit de resultaten van de analyse van de Cabauw-dataset, die de uitgebreidere dataset van de twee heeft opgeleverd, werd ook duidelijk dat opwaartse luchtstroom in de wolk een belangrijke rol speelt bij het stimuleren van aerosols tot druppels. Een mogelijke uitbreiding van de gepresenteerde methode omvat het verkrijgen van optische wolkuitdoving uit de UV-lidarmetingen. De methodiek kan zeer betrouwbare resultaten opleveren, met nauwe overeenkomsten met de gesimuleerde resultaten. Hierdoor kan de optische extinctie van de wolk worden gebruikt als een proxy van de eigenschappen van de wolk en kan

de beschreven methode voor het bewaken van aërosol-wolkinteracties ook worden toegepast op meetlocaties waar alleen UV-lidar en radiometers aanwezig zijn. Dit proefschrift toont aan dat het synergetisch gebruik van teledetectie-instrumenten vanaf de grond voortdurende en efficiënte monitoring van aërosol-wolkinteracties mogelijk maakt.

1

Introduction

1.1. Motivation

Global climate change is affecting people in more ways than ever. Quantifying the rate of it is becoming of interest not only for the scientists, but also for policy makers and the society in general. The Intergovernmental Panel on Climate Change (IPCC) regularly summarises the scientific achievements and gaps in the scientific progress of our understanding of those global changes. The importance of impact of clouds and aerosols on climate has been underlined since the first Assessment Report (AR1) published in 1990 [1]. The aim of this thesis is to propose a method to evaluate the impact of aerosols on cloud formation. The main goal of this method was to create a fast way of comparing the properties of the aerosols and clouds. Using these evaluation instruments that are widely accessible. In this manner it is possible to create a large area over which the method can be implemented. The chosen instruments also needed to be able to operate continuously so that the method can be used also for near real time monitoring of the aerosols and cloud conditions. The final set of the instrument chosen for this method consisted of lidar, radar and radiometer, all the instruments that are readily available in the cloud observing sites of the ACTRIS (Aerosol, Clouds and Trace Gases Research Infrastructure) network. With a wide geographical spread and continuous operation this method aims to contribute to decreasing the uncertainties present in the climate models due to the unaccounted for effect of aerosols and cloud interactions.

1.2. Aerosol - cloud interactions

1.2.1. What are aerosols?

Aerosols are a collection of solid or liquid particles suspended in a gaseous medium. Aerosols can come from numerous sources and form through different mechanisms, hence their chemical composition and size distribution vary greatly [2]. Aerosols can be divided based on the source of their origin in the atmosphere: those that are emitted directly to the atmosphere are known as the primary aerosol,

and those produced from the precursor gases in the atmosphere are called secondary. Primary aerosols are emitted into the atmosphere as particles. They can be of both organic and inorganic nature. Inorganic primary aerosols come mostly from sea spray, dust and volcanoes. They are relatively large (around 1 micrometer) and have a short lifetime in the atmosphere, typically a couple of days. The organic primary aerosols are mostly carbonaceous aerosol, organic carbon (OC) and solid black carbon (BC). They come into the atmosphere through combustion, from plant and microbial sources and through biomass burning. BC is the main primary aerosols that can be traced to anthropogenic sources. It comes mainly from combustion of fossil fuels and biomass. Secondary aerosols appear in the atmosphere from precursor gases through processes of condensation on pre-existing particles or by nucleation of new particles. They are composed of a mixture of compounds, mainly sulphate, nitrate and OC. The main source of the precursor gases is the fossil fuel combustion. The secondary contributors include biomass burning and emission of volatile organic compounds (VOCs). Huge amounts of primary and secondary aerosols can appear in the atmosphere through volcanic eruptions [3].

1.2.2. Influence of aerosols on climate

Direct effect

All types of aerosols present in the atmosphere scatter solar radiation. Some of the aerosol, mainly BC, mineral dust and some of the OC also have the ability to absorb solar radiation. The scattering aerosols influence climate by contributing to the cooling effect, as they increase the amount of solar radiation that is being reflected back from the Earth. Aerosols that are capable of strong absorption can contribute to the warming effect on the climate. As the atmosphere contains a mixture of both absorbing and scattering aerosol, their effect on the total Earth's energy budget varies depending on surface and cloud characteristics.

Indirect effects

Aerosols are indispensable for the process of cloud formation as they act as cloud condensation nuclei (CCN) or ice nuclei (IN). In the condition when the amount of liquid water content is fixed, an increase in CCN will lead to a formation of more cloud droplets. Those droplets though will be smaller and will lead to a number of cloud perturbations that may cause changes to the radiative budget. The main mechanisms of the smaller droplet size are presented on Figure 1.1.

The constant advancement in our understanding of the interactions between aerosols and clouds seems to be much more complex [5] than first reported cloud albedo effect [6] and cloud lifetime effect [7]. We know that in some situations the total radiative forcing of the cloud albedo effect (brightening of clouds due to a smaller cloud droplet size and thus increased cloud albedo) might be buffered by less cloud water being available in trade wind cumulus. In Stratocumulus clouds smaller droplet size causes clouds not only to be brighter but also suppresses drizzle, which further increases clouds cooling effect due to an increased lifetime of clouds and hence overcast [8]. Aerosols influence also deep convective clouds by transporting increased amounts of smaller ice particles to the anvils of such clouds.

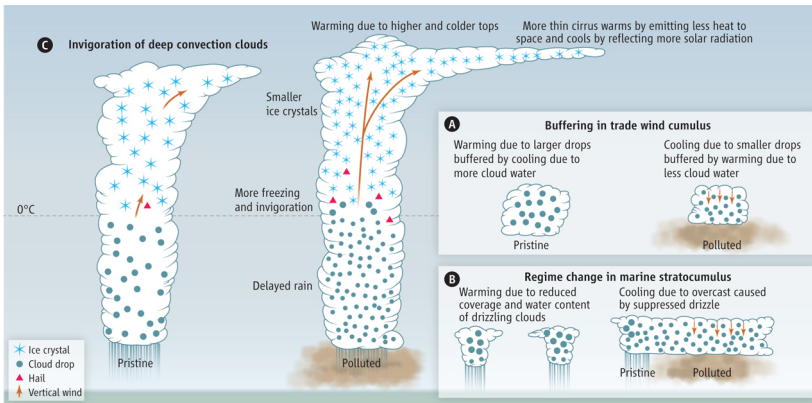


Figure 1.1: Effects of aerosols on the radiative properties of clouds. By nucleating a larger number of smaller cloud drops, aerosols affect cloud radiative forcing in various ways. (A) Buffering in onprecipitating clouds. The smaller drops evaporate faster and cause more mixing of ambient air into the cloud top, which further enhances evaporation. (B) Strong cooling. Pristine cloud cover breaks up by losing water to rain that further cleanses the air in a positive feedback loop. Aerosols suppressing precipitation prevent the breakup. (C) Larger and longer-lasting cirrus clouds. By delaying precipitation, aerosols can invigorate deep convective clouds and cause colder cloud tops that emit less thermal radiation. The smaller ice particles induced by the pollution aerosols precipitate more slowly from the anvils. This can cause larger and longer-lasting cirrus clouds, with opposite effects in the thermal and solar radiation. The net effect depends on the relative magnitudes [4].

The anvils become more expansive, higher and colder, which in turn leads to a warming effect by emitting less thermal radiation to space [9]. As clouds are very complex systems, it is difficult to account for those multiple effects, and the majority of studies focus only on a subset of suspected effects, trying to isolate very specific cases. In this study we focused on the effect of aerosols on the liquid water clouds as first described by Twomey [10].

1.2.3. Understanding aerosols - cloud interactions

The microphysical process leading to cloud formation through the activation of aerosols into cloud droplets is well described and understood [11]. Over the past decade there were many studies trying to quantify the impact of increased aerosols concentration on the cloud properties (e.g. [12, 13]). However when trying to understand the influence of aerosols on the formation of the liquid water clouds there are two major obstacles. First of them is the problem of entanglement of this process with other clouds processes such as aerosols effect on cloud dynamics or entrainment [14]. The second one is the mismatch between the scale at which the observations are being performed and at which the process is taking place [15, 16]. Satellite observations of the process provide global coverage that is essential for introducing the radiative forcing associated with aerosol-cloud interactions into the global climate models. Unfortunately observations of CCN with satellites are difficult [17]. On the other hand, in situ measurements are costly and provide only sparse samples, collected only during dedicated measurement campaigns. Ground-based

remote sensing, despite its inherent uncertainties, provides long-term records collected from simultaneous measurements of clouds and aerosols background below them.

1.3. This thesis

This thesis describes a method of monitoring aerosol-cloud interactions (further referred to as ACI method) with ground-based remote sensing instruments. It is structured as follows:

- Chapter 2 defines a ground-based remote sensing scheme for monitoring aerosol–cloud interactions. In this chapter the basic principles of the method are laid down along with an application of the method to pristine marine clouds.
- Chapter 3 describes a scheme for monitoring aerosol–cloud interactions at the CESAR Observatory in the Netherlands. It utilizes the method described in Chapter 2 and applies it to monitoring aerosol-cloud interaction over land in a continuous manner.
- Chapter 4 presents a method for estimating optical extinction of liquid water clouds in the cloud base region. The retrieved extinction can be used as a proxy of cloud microphysical properties in the aerosol-cloud monitoring scheme.
- Chapter 5 summarises the main results of the three previous chapters and proposes an outlook on future developments and applications.

References

- [1] I. W. G. I, *Climate Change 1990 The Science of Climate Change*, edited by J. Houghton, G. Jenkins, and J. Ephraums (The Intergovernmental Panel on Climate Change, 1996).
- [2] J. P. Putaud, R. Van Dingenen, A. Alastuey, H. Bauer, W. Birmili, J. Cyrus, H. Flentje, S. Fuzzi, R. Gehrig, H. C. Hansson, R. M. Harrison, H. Herrmann, R. Hittenberger, C. Hüglin, A. M. Jones, A. Kasper-Giebl, G. Kiss, A. Kousa, T. A. Kuhlbusch, G. Löschau, W. Maenhaut, A. Molnar, T. Moreno, J. Pekkanen, C. Perrino, M. Pitz, H. Puxbaum, X. Querol, S. Rodriguez, I. Salma, J. Schwarz, J. Smolik, J. Schneider, G. Spindler, H. ten Brink, J. Tursic, M. Viana, A. Wiedensohler, and F. Raes, *A European aerosol phenomenology - 3: Physical and chemical characteristics of particulate matter from 60 rural, urban, and kerbside sites across Europe*, *Atmospheric Environment* **44**, 1308 (2010).
- [3] J. Boulon, K. Sellegri, M. Hervo, and P. Laj, *Observations of nucleation of new particles in a volcanic plume*, *Proceedings of the National Academy of Sciences of the United States of America* **108**, 12223 (2011).
- [4] D. Rosenfeld, S. Sherwood, R. Wood, and L. Donner, *Climate effects of aerosol-cloud interactions*, (2014).
- [5] I. S. Isaksen, C. Granier, G. Myhre, T. Berntsen, S. B. Dalsøren, M. Gauss, Z. Klimont, R. Benestad, P. Bousquet, W. Collins, T. Cox, V. Eyring, D. Fowler, S. Fuzzi, P. Jöckel, P. Laj, U. Lohmann, M. Maione, P. Monks, A. S. Prevot, F. Raes, A. Richter, B. Rognerud, M. Schulz, D. Shindell, D. Stevenson, T. Storelvmo, W. C. Wang, M. van Weele, M. Wild, and D. J. Wuebbles, *Atmospheric Composition Change: Climate-Chemistry Interactions*, in *The Future of the World's Climate* (Elsevier, 2012) pp. 309–365.
- [6] S. Twomey, *Pollution and the planetary albedo*, *Atmospheric Environment* (1967) **8**, 1251 (1974).
- [7] B. A. Albrecht, D. A. Randall, and S. Nicholls, *Observations of marine stratocumulus clouds during FIRE*, *Bulletin - American Meteorological Society* **69**, 618 (1988).
- [8] A. S. Ackerman, O. B. Toon, and P. V. Hobbs, *Dissipation of marine stratiform clouds and collapse of the marine boundary layer due to the depletion of cloud condensation nuclei by clouds*, *Science* **262**, 226 (1993).
- [9] I. Koren, L. A. Remer, O. Altaratz, J. V. Martins, and A. Davidi, *Aerosol-induced changes of convective cloud anvils produce strong climate warming*, *Atmospheric Chemistry and Physics* **10**, 5001 (2010).
- [10] S. Twomey, *The Influence of Pollution on the Shortwave Albedo of Clouds*, *J. Atmos. Sci.* **34**, 1149 (1977).

- [11] D. Lamb and J. Verlinde, *Physics and Chemistry of Clouds* (Cambridge University Press, 2011).
- [12] G. Feingold, *First measurements of the Twomey indirect effect using ground-based remote sensors*, [Geophysical Research Letters](#) **30**, 19 (2003).
- [13] A. McComiskey, G. Feingold, a. S. Frisch, D. D. Turner, M. a. Miller, J. C. Chiu, Q. Min, and J. a. Ogren, *An assessment of aerosol-cloud interactions in marine stratus clouds based on surface remote sensing*, [Journal of Geophysical Research: Atmospheres](#) **114**, 1 (2009).
- [14] G. Feingold, A. McComiskey, T. Yamaguchi, J. S. Johnson, K. S. Carslaw, and K. S. Schmidt, *New approaches to quantifying aerosol influence on the cloud radiative effect*. [Proceedings of the National Academy of Sciences of the United States of America](#) , 1514035112 (2016).
- [15] A. McComiskey and G. Feingold, *The scale problem in quantifying aerosol indirect effects*, [Atmospheric Chemistry and Physics](#) **12**, 1031 (2012).
- [16] J. Mülmenstädt and G. Feingold, *The Radiative Forcing of Aerosol–Cloud Interactions in Liquid Clouds: Wrestling and Embracing Uncertainty*, (2018).
- [17] J. H. Seinfeld, C. Bretherton, K. S. Carslaw, H. Coe, P. J. DeMott, E. J. Dunlea, G. Feingold, S. Ghan, A. B. Guenther, R. Kahn, I. Kraucunas, S. M. Kreidenweis, M. J. Molina, A. Nenes, J. E. Penner, K. A. Prather, V. Ramanathan, V. Ramaswamy, P. J. Rasch, A. R. Ravishankara, D. Rosenfeld, G. Stephens, and R. Wood, *Improving our fundamental understanding of the role of aerosol-cloud interactions in the climate system*, [Proceedings of the National Academy of Sciences of the United States of America](#) **113**, 5781 (2016).

2

Ground-based remote sensing scheme for monitoring aerosol-cloud interactions

Karolina Sarna, H.W.J. Russchenberg

A new method for continuous observation of aerosol-cloud interactions with ground-based remote sensing instruments is presented. The main goal of this method is to enable the monitoring of the change of the cloud droplet size due to the change in the aerosols concentration. We use high resolution measurements from lidar, radar and radiometer, which allow us to collect and compare data continuously. This method is based on a standardised data format from Cloudnet and can be implemented at any observatory where the Cloudnet data set is available. Two example study cases were chosen from the Atmospheric Radiation Measurement (ARM) Program deployment at Graciosa Island, Azores, Portugal in 2009 to present the method. We use the cloud droplet effective radius (r_e) to represent cloud microphysical properties and an integrated value of the Attenuated Backscatter Coefficient (ATB) below the cloud to represent the aerosols concentration. All data from each study case is divided into bins of the Liquid Water Path (LWP), each 10 g/m^2 wide. For every LWP bin we present the correlation coefficient between $\ln r_e$ and $\ln \text{ATB}$, as well as ACI_r (defined as $\text{ACI}_r = -d \ln r_e / d \ln \text{ATB}$, change

This chapter has been published in Atmospheric Measurement Techniques **9**, 1039–1050, 2016 [1].

in cloud drop effective radius with aerosols concentration). Obtained values of ACI_r are in the range 0.01–0.1. We show that ground-based remote sensing instruments used in synergy can efficiently and continuously monitor aerosol-cloud interactions.

2.1. Introduction

The interactions of low-level liquid water clouds with aerosols are considered one of the main sources of uncertainty in climate change predictions. According to the Fifth Assessment Report (AR5) of the Intergovernmental Panel on Climate Change [2], clouds and the effects of aerosols on their macro- and micro-structure continue to contribute to the largest uncertainty in the estimation and interpretation of the Earth's energy budget. Low-level liquid water clouds impact mainly the shortwave radiation budget, as it is mostly sensitive to the cloud albedo. The effect of aerosols concentration on cloud reflectance is often referred to as the albedo effect [3]. The albedo effect is based on the close relation between the aerosols concentration and the cloud droplet concentration.

An ample number of studies have been made to quantify the impact of aerosols concentration on cloud microphysical properties. Studies focusing on low-level liquid water clouds are often based on different methods and instruments. Because of this the temporal and spatial resolution vary significantly. Observational studies of the aerosols effect on clouds use surface remote sensing instruments at specific locations [e.g., 4, 5] or rely on a combination of both surface remote sensing and aircraft in-situ observations [e.g., 6–8]. To characterise the aerosols effect on a global scale, many researches focus on the satellite remote sensing observations [e.g., 9]. McComiskey and Feingold [10] summarised the broad scope of different methods and scales used. They concluded that a single measure of aerosol-cloud interactions (ACI) used in climate model estimates of the radiative forcing yields widely fluctuating results. ACI is a single measure derived from observational data from varying scales and different assemblies of instruments. Further, they concluded that ACI_r (defined as $ACI_r = -d \ln r_e / d \ln \alpha$, change in cloud drop effective radius with aerosols concentration) is only useful at a small scale measurements. That way it can be measured at a scale of the process it represents, that is at a microphysical scale. Microphysical changes in cloud and aerosols can be captured by either *in situ* measurements or point-based remote sensing observations from the ground with a high temporal resolution. Therefore in this paper we focus on a new methodology that allows to continuously observe ACI with ground-based remote sensing instruments over multiple locations.

We present an approach for monitoring aerosol-cloud interactions with ground-based remote sensing instruments. We use specifically zenith-pointing cloud radar, lidar and microwave radiometer to characterise cloud microphysical properties and the aerosols concentration in the same column. Thanks to the unique capabilities of the ground-based remote sensors data can be collected and compared continuously. Due to the fine height and time resolution available cloud and aerosols properties are observed in the same air column. We developed the monitoring scheme on the basis of the standardised data format from Cloudnet [11]. The method described here can be implemented on multiple ground-based observational sites (e.g., the European ACTRIS network - Aerosol, Clouds and Trace gases Research InfraStructure and the US Atmospheric Radiation Measurement (ARM) Program - both databases provide Cloudnet data set), where a long term database of measurements already exists. This will allow to perform statistical calculations of ACI

for different locations.

The structure of this paper is as follows: first, we provide a description of the methodology for estimating the relationship between the aerosols concentration below the cloud base and the cloud droplet concentration and the droplet sizes in the cloud base region. We describe the combination of instruments and proxies used in the method. Then we show two example study cases from the ARM Mobile Facility at Graciosa Island at the Azores, Portugal. Finally, we discuss the possibilities of implementing this method over the network of cloud profiling observatories in Europe.

2.2. Quantifying interactions between aerosols and cloud

Very often in the literature the term aerosol-cloud interactions is associated with quantification of the impact of aerosols on cloud albedo. This relation was first postulated by Twomey [3]. Through experimental studies he showed that the number concentration of aerosols (N_a) below the cloud is monotonically related to the cloud droplet number concentration (N_d):

$$N_d \propto N_a^\gamma. \quad (2.1)$$

[12], where γ is the proportionality factor. The value of γ varies between 0.7 and 0.8 in different experimental studies [3, 13], and the theoretical bounds are between 0 and 1. N_a and N_d are not directly proportional. The increase in the concentration of aerosols that can be activated into cloud droplets can lead to the lowering of the maximum relative humidity in the cloud base region [3]. Twomey [14] further derived a theoretical relationship between the aerosols concentration and cloud albedo. He proposed that, an increased aerosols concentration will lead to an increased cloud droplet concentration and a smaller effective radius of cloud droplets (r_e). A smaller effective radius of cloud droplets will result in a brighter cloud and an increased cloud albedo. This is only true if the amount of available water, represented by the Liquid Water Path (LWP), is constant.

The cloud optical thickness (τ_d) is a function of both the cloud droplet concentration and cloud effective radius. Thus, we can assume that the optical thickness will be rising with the increase of the droplet concentration,

$$\tau_d \propto N_d^{1/3} \quad (2.2)$$

[3], and the decrease of the droplet radius:

$$\tau_d \propto \frac{LWP}{r_e} \quad (2.3)$$

[15].

Theoretical relationships between variables in Equations (2.1),(2.2) and (2.3) led to the formulation of a relation between the aerosols optical thickness (τ_a) (as τ_a is a function of the aerosols number concentration (N_a)) and the effective radius of cloud droplets (r_e):

$$r_e \propto \tau_a^{-\gamma/3} \quad (2.4)$$

[16], which is a basic theoretical relation used presently to quantify the effect described by Twomey [3]. In order to empirically quantify the aerosol-cloud interactions Feingold *et al.* [17] introduced the indirect effect index (*IE*), later referred to as the ACI (Aerosol-Cloud Interactions),

$$IE = ACI_r = - \left. \frac{d \ln r_e}{d \ln \alpha} \right|_{LWP} \quad 0 < ACI_r < 0.33, \quad (2.5)$$

and

$$IE = ACI_\tau = \left. \frac{d \ln \tau_d}{d \ln \alpha} \right|_{LWP} \quad 0 < ACI_\tau < 0.33, \quad (2.6)$$

or

$$IE = ACI_N = \frac{d \ln N_d}{d \ln \alpha} \quad 0 < ACI_N < 1, \quad (2.7)$$

where α is an observed proxy of the aerosols concentration. Parameters such as aerosols number concentration (N_a), aerosols optical thickness (τ_a) or Aerosol Index (*AI*), which is a product of τ_a and Angström exponent, were used to represent the aerosols concentration in different studies. Note that ACI_N is not bounded by the value of LWP and is derived directly from Eq. 2.1.

In mathematical terms, ACI_r , ACI_τ and ACI_N are represented by a slope of a linear regression between a logarithm of a cloud property (dependent variable) and a logarithm of an aerosols property (independent variable). Thus, we can write ACI_r as

$$ACI_r = R_{aerosol,cloud} \frac{S_{cloud}}{S_{aerosol}} \quad (2.8)$$

[10], where $R_{aerosol,cloud}$ is the Pearson Product-Moment Correlation Coefficient between the logarithm of aerosols property and the logarithm of the cloud property, S_{cloud} is the standard deviation of the cloud property and $S_{aerosol}$ is the logarithm of the aerosols property.

It is important to note that in order to derive Eq. (2.2) a series of assumptions was made. Twomey and Warner [12] assumed that cloud is homogeneous. It allowed them to apply properties of the cloud base area to the whole cloud. For a cloud in an early formation stage the cloud droplet concentration is decided mainly by the number of cloud condensation nuclei in the cloud base area. By assuming that cloud is homogeneous, the same is true for the whole cloud. Further, Twomey assumed that both cloud droplet number concentration and aerosols optical thickness are directly proportional to an increasing aerosols concentration. This means that he considered all components in the aerosols to increase together and at the same proportion. The combination of these assumptions greatly minimises the amount of observational study cases where the relation from Eq. (2.2) can be applied.

Another important and often omitted factor is: the cloud droplet concentration (N_d) is modified by mixing, collision, coalescence and evaporation within the cloud. However, at the area close to the cloud base, where the cloud is at the early formation stage, the initial N_d is determined by the amount of nuclei able to activate into cloud droplets at or below the maximum supersaturation in the cloudy air [12]. This

means that the aerosols concentration should be related to the number concentration of cloud droplets in the cloud base area in observational studies, as translation of this relationship to the whole clouds requires to assume that cloud is homogeneous. And that is rarely the case.

In this study we focus on the aerosol-cloud interactions as an approximation of the nucleation process without relating it to the cloud albedo. We design a method that enables daily monitoring of the microphysical processes between aerosols and clouds. We quantify the relation between cloud and aerosols properties with statistical parameters. We assume that the aerosols concentration below the cloud is monotonically related to the cloud droplet concentration in the cloud base region (Eq. 2.1) and that the increase of the cloud droplet concentration leads to a decrease of the cloud droplet size. We perform a logarithmic transformation of both aerosols and cloud properties. Thus, the quantities we use for determining the relation between aerosols concentration and cloud droplet size are the natural logarithm of the Attenuated Backscatter Coefficient ($\ln ATB$) and the natural logarithm of the cloud droplet effective radius ($\ln r_e$) - see Section 2.2.1.

We use the Pearson Product-Moment Correlation Coefficient, R , to establish how dependent the cloud drop size is on the aerosols concentration. The sign of the correlation coefficient will show if the increasing concentration of aerosols actually decreases with the cloud droplet size. We further calculate ACI_r (Eq. 2.5), which as we mentioned before represents the slope of the regression line between the cloud droplet effective radius (r_e) and the aerosols concentration. ACI_r is important to estimate the proportionality factor γ as defined in Eq. 2.1 and 2.4. We also calculate the Coefficient of Determination, r^2 , which suggests the percentage of the variability in cloud droplet size that can be explained by changes in aerosols concentration. We want to analyse data daily when the specific conditions are present (see Section 2.3.2) and divide data into small bins of Liquid Water Path (LWP) to approximate the conditions in each bin to a constant LWP , as postulated by Twomey [14].

2.2.1. Aerosols and Cloud Properties Proxies

Clouds are formed when aerosols particles are activated into cloud droplets. Activation is a change from stable to unstable growth due to the increase of the ambient humidity. When haze droplets reach critical radius [18], they are transformed into cloud droplets. When a higher concentration of the aerosols particles is present, the competition for the excess water vapour will be greater and thus, the resulting cloud droplets will be smaller [19].

In low level liquid water clouds, in particular Stratocumulus, the number of the activated droplets is approaching the concentration of the aerosols accumulation mode (particles between $0.1 \mu\text{m}$ and $1 \mu\text{m}$), making that concentration itself the primary determinant of the cloud droplet concentration [e.g., 20, 21]. Based on an adiabatic cloud parcel model representing the hygroscopic growth of CCN and droplet condensation, Feingold [16] concluded that aerosols number concentration (N_a) contributes most significantly to aerosols effects on clouds. Other aerosols parameters, such as size, breadth of the aerosols size distribution and its chemical composition are of a secondary importance.

2.2.2. Relation between Aerosols and Cloud Proxies

The strong relation between aerosols concentration and cloud droplet concentration (Eq. 2.1) is postulated both by theory and observations. We expect to see an inverse relationship between the aerosols concentration and cloud droplets size. With the increase of the aerosols concentration, the cloud droplet size is expected to decrease while at the same time the cloud droplet concentration is expected to increase. This is true if the amount of available water, LWP, is kept constant.

2.3. Methodology

2.3.1. Instrumentation and Data set

Very often collocated measurements of aerosols and cloud properties are not available at a similar time resolution. Alternatively, data are being collected only during specific measurements campaigns. This does not allow for a continuous monitoring of aerosol-cloud interactions. To gain a better understanding of the aerosols impact on cloud microphysical properties we need to have continuous measurements, in different meteorological conditions and over multiple locations. Also, to eliminate rapid variation in the meteorological conditions we want to evaluate data daily. Ground-based remote sensing instruments are able to provide continuous measurements. They can provide a fine temporal and height resolution measurements that can be used to monitor aerosol-cloud interactions. The goal of our method is to monitor the interactions between aerosols and clouds. We combine measurements from three separate instruments: cloud radar, lidar and microwave radiometer. This combination of instruments can capture and monitor the influence of a changing aerosols concentration on the cloud microphysical properties. We used the Cloudnet data set, which provides a set of high quality measurements from radar, lidar and a microwave radiometer. The specification of all three instruments may vary slightly per Cloudnet site, but the retrieval algorithms are always the same. The detailed specification of instruments used in this study is presented in Section 2.4. Additionally, each pixel of the height-time grid of the Cloudnet data set is categorised in terms of the presence of liquid droplets (cloud, rain or drizzle), ice, insects or aerosol. This categorisation is a specific product of Cloudnet data set [22] and was designed to facilitated the retrievals of cloud microphysical properties. This categorisation product allows us to construct an algorithm that can be applied to specific targets only, liquid water cloud droplets and aerosol, and provides an easy way of selecting data based on a set of selection criteria (Sec. 2.3.2).

Aerosols Number Concentration

Numerous proxies have been used in the past to represent the aerosols concentration. In this method we aim at using continuous measurements with a high spatial and temporal resolution. Such data set is available from a lidar, in the set-up of this research specifically a Vaisala CT25K ceilometer operating at 905 nm. Several research indicate that a ceilometer can be used as a quantitative aerosols measurement instrument [23, 24]. Backscatter from ceilometers (β) can be approximated

as:

$$\beta \approx \int_0^{\infty} N_a(D_a) D_a^2 dD_a, \quad (2.9)$$

where N_a is the number concentration of aerosols and D_a is the aerosols diameter. The averaged β shows good correlations with the *in situ* measurements of the mass concentration of the particulate matter up to 10 μm (PM10) and smaller than 2.5 μm (PM2.5) [25].

In this method we use a column-integrated value of the Attenuated Backscatter Coefficient (*ATB*) in order to represent the whole column of aerosols below the cloud. We only consider well-mixed conditions (Section 2.3.2). Specifically, we only look into single-layer clouds on top of the boundary layer with the cloud base below 2000 m. Data are integrated from the level of a complete overlap (minimum height where the cross-section of the lidar laser beam is completely in the field of view of the receiver's telescope [26]), which is 120 m in our study, up to 300 m below the cloud base. The distance from the cloud minimises the amount of cloud and haze droplets or wet aerosols mixed through the considered aerosols background. The specific distance of 300 m was used in other studies based on ground-based lidar measurements [27]. Very often a set height of the aerosols concentration proxy is used in the aerosol-cloud interaction studies (e.g. Raman lidar extinction at 350 m [28]). We compared aerosols property (*ATB*) and cloud property (cloud drop effective radius - r_e) at a set height, 350 m from the ground for the *ATB*, and a mean value of r_e through the cloud, with the *ATB* and r_e set at a specific distance from the cloud base (and the cloud base height is seldom constant), 300 m below the cloud for *ATB* and 85 m above the cloud base for r_e . We found that by considering the level of aerosols proxy (*ATB*) and cloud proxy (r_e) at a set distance from the cloud base the dependence of cloud properties on aerosols concentration is bigger. Explicitly, the correlation coefficient, R , has a higher absolute value. Therefore we use a height based on a set distance from the cloud base for both aerosols and cloud properties in this study.

Note that Cloudnet ceilometers are calibrated with the method of O'Connor *et al.* [29] which introduces a calibration uncertainty of up to 10%. The precision of the measurements is difficult to estimate as the internal processing algorithms are proprietary. A single value of 0.5 dB is used for all pixels [22].

Cloud Droplet Size and Number Concentration

Aerosol-cloud interactions are described as the response of the microphysical properties of the cloud to the change of the aerosols concentration. The cloud properties that we are specifically interested in are the cloud droplet size and the number concentration of the droplets. Both these variables are obtained through a retrieval of cloud microphysical properties from measurements.

We apply a method according to Frisch *et al.* [30] to retrieve the cloud droplet concentration (N_d) and the cloud droplet effective radius (r_e). This retrieval method uses observations from cloud radar and microwave radiometer (MWR). Assuming that N_d and a gamma cloud droplet distribution, with a fixed distribution shape (ν), are constant with height, the r_e can be derived from the Radar Reflectivity Factor

(Z) and the MWR retrieved LWP :

$$r_e(h) = \left(\frac{(v+2)^3}{(v+3)(v+4)(v+5)} \right)^{\frac{1}{3}} \left(\frac{\pi \rho_w \sum_{i=1}^n Z^{\frac{1}{2}}(h_i) \Delta h}{48LWP} \right)^{\frac{1}{3}} Z^{\frac{1}{6}}(h), \quad (2.10)$$

where ρ_w is the density of liquid water (10^6 gm^{-3}), Δh is the length of the radar range gate, $Z(h_i)$ is the reflectivity factor at the i^{th} radar measured gate and n represents the number of the in-cloud radar-measured gates. The cloud droplet number concentration (N_d) is calculated from the following formula:

$$N_d = \left(\frac{(v+3)(v+4)(v+5)}{v(v+1)(v+2)} \right) \left(\frac{6LWP}{\pi \rho_w \sum_{i=1}^n Z^{\frac{1}{2}}(h_i) \Delta h} \right). \quad (2.11)$$

Both of these retrieved properties have been evaluated against other methods in [31]. The comparison of different retrieved microphysical cloud properties revealed that r_e is the parameter least affected by the instrumental errors of MWR and radar. The estimated uncertainties in r_e are about 10-15 % and in N_d around 40-60 %. In both proxies the uncertainties are due to instrument errors and algorithm assumptions. The main algorithm assumptions include: (1) the droplet size distribution is approximated by a mono-modal gamma distribution, (2) the moments of the droplet size distribution are correlated among each other and (3) the droplet concentration and droplet size distribution shape parameter remain constant with height in each profile.

Following [31], the gamma cloud droplet distribution shape parameter is set to 8.7. This value is obtained from the ratio between the third and second moments of the droplet distribution and has been found in reanalysis of the in-situ observations of Stratocumulus clouds [32].

Similarly to the aerosols proxy, we compare the r_e at a set distance from the cloud base. We set this distance at 85 m above the cloud base detected from the lidar measurements. Lidar can detect the cloud base height more precisely than radar, that difference can be up to two range gates. Hence we use the distance of 85 m, which is equal to two range gates, to ensure that the cloud is detected by both instruments.

2.3.2. Data Selection Criteria

Clouds are complicated systems with many processes taking place at the same time. Singling out a small microphysical process is difficult. Data needs to be limited by implementing a number of filters. Firstly, this monitoring scheme applies only to liquid water clouds on top of the boundary layer in well-mixed conditions, where the cloud base is located below 2000 m. This limitation ensures that the cloud is not decoupled from the boundary layer and the aerosols background below the cloud [28]. Secondly, we can only consider data where no precipitation is present, including drizzle, as it can obscure the formative stage of a cloud [4]. We use the Cloudnet categorisation data for the classification of the observed targets. This

scheme relies on the measurements from three separate instruments. Only profiles where all three instruments provide good quality data can be analysed. Data quality is classified in the Cloudnet data set in a similar way to the categorisation product. We can therefore easily filter data where a problem with the measurements was detected.

Some larger scale factors, such as boundary layer dynamics or variations in temperature, pressure or humidity, can influence changes in the cloud. We ensure similar meteorological conditions by analysing aerosols and cloud properties on a daily basis. This minimises the influence of variations in general weather conditions. However, the transition between meteorological conditions can happen within a day and often even at a smaller time scale. To account for this kind of daily changes we use filters of the meteorological conditions, namely temperature, pressure and specific humidity. For each parameter we calculate a mean value and a standard deviation, if the standard deviation is below 10% of the mean value we consider that as similar meteorological conditions. We use the integrated value of *ATB* as a proxy of aerosols concentration. As we mentioned before, we integrate *ATB* in column from 120 m above the ground (level of complete overlap) to 300 m below the cloud base height. This limits the possible cloud base height to above 500 m above the ground level, if the *ATB* is to be integrated over at least two ranges.

We also apply a constraint on *LWP* to isolate the aerosols activation process from different interactions that can happen at the same time. Daily data sets are divided into profiles where the value of *LWP* is similar. We divide the data into bins of *LWP* of 10 gm^{-2} . Creating even smaller bins is difficult due to the limited data points. We only consider *LWP* bins where the total amount of data points is above 20. *LWP* should be above 30 gm^{-2} and below 150 gm^{-2} . Values below 30 gm^{-2} are disregarded because of the uncertainty of *LWP* calculated from MWR, which is around 15 gm^{-2} [33]. The values above 150 gm^{-2} are excluded to avoid precipitating clouds. The analysis of an aggregated data set grouped by varying meteorological conditions (as defined above) would be a good way of getting a better understanding of aerosol-cloud interactions drivers. Such a study can be made with the monitoring method presented in this study but is beyond the scope of this manuscript.

2.4. Application of the method to observations from Graciosa Island, Azores

We present here two example study cases of the practical application of the method described above. The deployment of the Atmospheric Radiation Measurement Program (ARM) Mobile Facility at Graciosa Island, Azores in 2009 and 2010 provides a comprehensive data set for assessing aerosols effects on low-level liquid water clouds. Boundary layer clouds were the most frequently observed cloud type (40–50%) with the maximum occurrence during the summer and fall months under the presence of anticyclonic conditions [34]. The instruments we use in this study are a W-band ARM Cloud Radar (WACR) operating at 95 GHz [35], a laser ceilometer Vaisala CT25K operating at 905 nm and a two-channel microwave radiometer (MWR) operating at 23 GHz and 31.4 GHz. Data from this campaign is available in the standardised Cloudnet format, which is the basis of calculations presented

Table 2.1: Cloud and Aerosol Properties Measured or Derived From the Observations at the Graciosa Island, Azores.

Measured Quantity	Definition	Instrument(s)
Cloud Liquid Water Path	LWP [gm^{-2}]	MWR
Radar Reflectivity Factor	Z [dBZ or m^6m^{-3}]	WACR
Cloud Droplet Effective Radius	r_e [μm] (see Eq. 2.10)	WACR/MWR
Cloud Droplet Number Concentration	N_d [cm^{-3}] (see Eq. 2.11)	WACR/MWR
Attenuated Backscatter Coefficient	ATB [$\text{m}^{-1}\text{sr}^{-1}$]	Vaisala CT25K

here. The Cloudnet data set is re-gridded to the vertical resolution of the radar (42.86 m) and the time resolution of the radiometer (30 s). Table 2.1 summarises all measurements and all products derived for the data analysis.

Based on the data selection criteria presented in the section above we identified two study cases for testing the method: 3 November 2009 and 29 November 2009. Both cases showed only a small variability of the LWP which enabled distribution of data into small bins of LWP gm^{-2} . The station was located at the North-East shore of the island, situated upwind in order to reduce the impact of the island. The NOAA HYSPLIT back trajectory model [36] indicated that the aerosols for the selected days were coming from marine sources. This single source of aerosols allowed us to test the method without adding the extra complexity of a multiple aerosols sources background. We chose two study cases from the same season, with similar meteorological conditions. Cases vary in the cloud base height and in the aerosols loading.

2.4.1. Study case from 3 November 2009

The conditions on 3 November 2009 were characterised by a northerly wind of about 2.5 ms^{-1} in the boundary layer. The cloud cover was persisting the whole day, with periods of drizzle and heavy rain after 1800 UTC. Precipitation-free periods were identified between 0000 UTC and 0500 UTC, with a second short period between 1330 UTC and 1500 UTC, set after a light precipitation event (Fig. 2.1). Based on the Cloudnet categorisation and the measurements from WACR and MWR, only data in these two periods were analysed on that day. $LWPs$ in the selected periods ranged from 15 gm^{-2} to 130 gm^{-2} . As few data points were available with LWP above 90 gm^{-2} , we limit the data analysed to a LWP between 30 gm^{-2} and 90 gm^{-2} . The cloud base was located around 800 m above ground level (AGL) between 0000 UTC and 0500 UTC and around 500 m AGL between 1330 UTC and 1500 UTC.

Figure 2.2 presents the time-height cross section of the retrieved microphysical cloud properties. Only data from time steps meeting the data selection criteria are calculated. In the chosen periods r_e varies from $3 \mu\text{m}$ to $7 \mu\text{m}$, with a mean radius $5 \mu\text{m}$ and a standard deviation of $0.75 \mu\text{m}$. N_d ranges in the selected periods from 150 to 1700 cm^{-3} . Some values are much higher than the observational data for

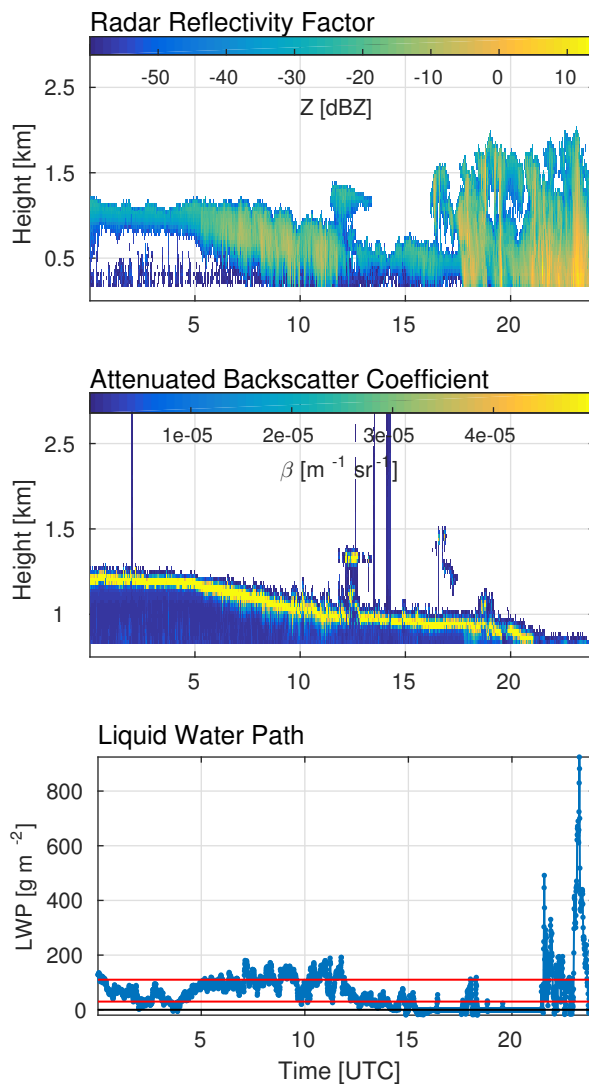


Figure 2.1: The time-height cross section of the Radar Reflectivity Factor from WACR, the Attenuated Backscatter Coefficient from Vaisala CT25K and the Liquid Water Path from MWR for a full day of measurements on 3 November 2009.

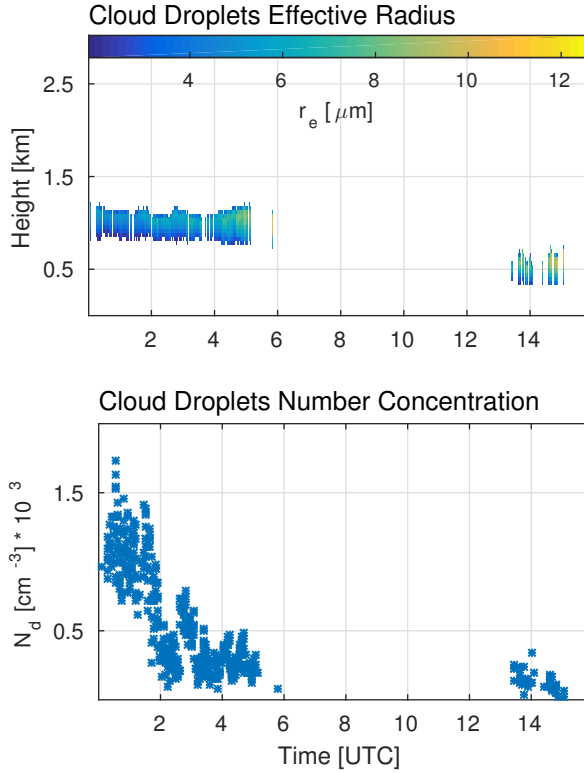


Figure 2.2: The time-height cross section of the Cloud Droplet Effective Radius (r_e) calculated from WACR and MWR measurements (Eq. (2.10)) and the Cloud Droplet Number Concentration (N_d) calculated from Eq. (2.11) from 3 November 2009. Data are only retrieved in the time steps when the data selection criteria are met.

Stratocumulus. N_d rarely exceeds 500 cm^{-3} and is generally lower (200 to 300 cm^{-3}) for marine Stratocumulus [20].

Aerosol background (represented by ATB) in the selected periods is variable with the mean value $0.64 \times 10^{-3} \text{ sr}^{-1}$ and a standard deviation of $0.18 \times 10^{-3} \text{ sr}^{-1}$. ATB in the period between 1330 UTC and 1500 UTC is significantly lower, mainly because it was followed by a period of precipitation and the cloud base was located considerably lower than in the first period.

All data points available on 3 November 2009 are divided into bins based on the value of the LWP which ranges from 30 to 90 gm^{-2} . Data were divided into 6 separate bins, each covering 10 gm^{-2} . Figure 2.3 presents relation between the integrated attenuated backscatter ATB and cloud droplet effective radius r_e . The calculated values of the correlation coefficient, R and ACI_r are presented for every bin. Both R and ACI_r are calculated for the $\ln ATB$ and $\ln r_e$ (Eq. 2.5).

Table 2.2 summarises values of R , ACI_r and the coefficient of determination, r^2 ,

Table 2.2: ACI_r (Eq. 2.5 and the statistical parameters calculated between $\ln(r_e)$ and $\ln(ATB)$, namely Pearson-Product Moment Correlation Coefficient, R , and the Coefficient of Determination, r^2 and the number of observations within the LWP bins, n , for two study cases from Graciosa Island at the Azores (3 and 29 November 2009).

LWP bin	3 November 2009				29 November 2009			
	ACI_r	R	r^2	n	ACI_r	R	r^2	n
$30 < LWP < 40$	0.01	-0.09	0.01	63	0.08	-0.50	0.25	45
$40 < LWP < 50$	0.06	-0.36	0.13	34	0.08	-0.52	0.27	63
$50 < LWP < 60$	0.06	-0.41	0.16	49	0.07	-0.56	0.31	67
$60 < LWP < 70$	0.04	-0.30	0.09	92	0.09	-0.65	0.42	96
$70 < LWP < 80$	0.00	-0.03	0.00	50	0.05	-0.39	0.16	98
$80 < LWP < 90$	0.08	-0.26	0.07	32	0.03	-0.27	0.07	39

for every LWP bin. The coefficient of determination, r^2 , suggests the percentage of the variability in cloud droplet size that can be explained by changes in aerosols concentrations. Note that both R and ACI_r values are highest for 3 November 2009 in the LWP range from 40 to 70 gm^{-2} . This may indicate that aerosol-cloud interactions representing the activation process are more significant only for the lower LWP values and for the higher values of LWP other processes, such as collision and coalescence of cloud droplets or cloud top cooling, may play a more important role. Another possible explanation can be the presence of drizzle when LWP is above 70 gm^{-2} . Some studies suggest that marine Stratocumulus clouds can form drizzle particles at LWP values as low as 75 to 100 gm^{-2} [34].

Figure 2.4 shows the relation between the integrated attenuated backscatter, ATB , and the cloud droplet number concentration, N_d , together with the corresponding R and ACI_N (Eq. 2.7). Cloud droplet number concentration increases with the increase of aerosols concentration (represented by ATB) as expected by the aerosol-cloud interactions.

2.4.2. Study case from 29 November 2009

On 29 November 2009 a northerly wind of about 2 ms^{-1} in the boundary layer persisted most of the day. Periods of drizzle and rain were occurring throughout the day, with a heavy precipitation after 1500 UTC. Therefore we only consider data before 1500 UTC.

The cloud base was located around 1600 m AGL (Fig. 2.5). Periods between 0000 UTC to 0300 UTC, 0530 UTC to 0600 UTC and 0830 UTC to 1400 UTC correspond with the data selection criteria. In all cases, the categorisation provided by Cloud-net identifies that the cloud layer consists of liquid water cloud and aerosols only. LWP in the selected periods varies between 15 gm^{-2} and 150 gm^{-2} . As there are few data points available with LWP above 90 gm^{-2} we limit the data analysed to a LWP between 30 gm^{-2} and 90 gm^{-2} .

Figure 2.6 shows the retrieved properties in periods corresponding to our data selection criteria. In the selected periods N_d varies from 55 to 1900 cm^{-3} , with a

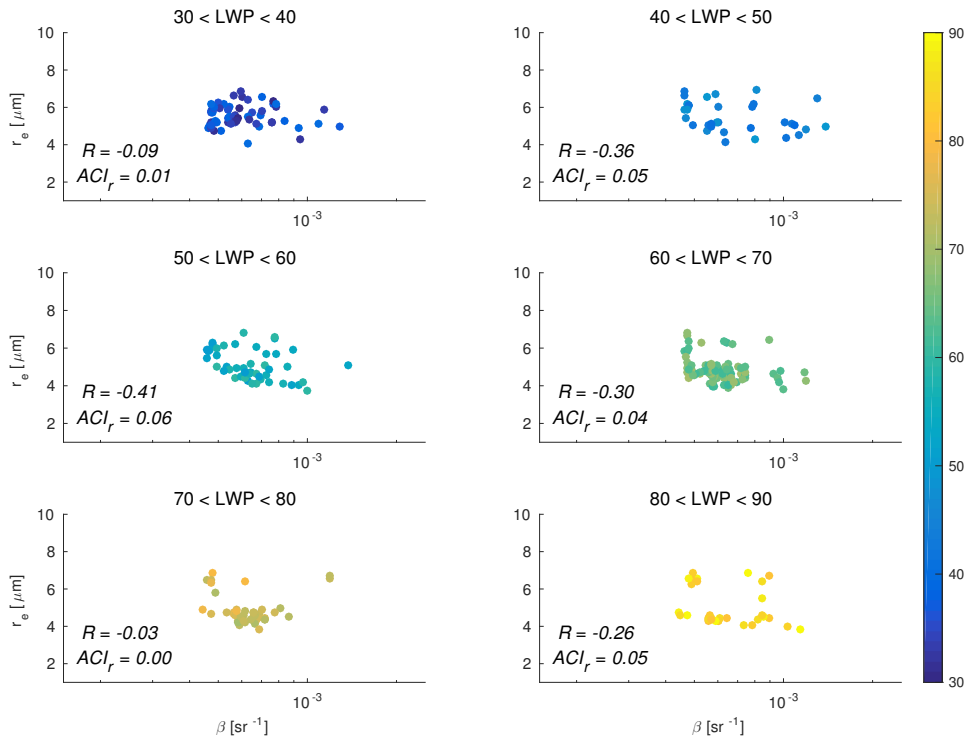


Figure 2.3: The values of the effective radius r_e derived from WACR and MWR measurements are plotted versus the integrated attenuated backscatter ATB measured by Vaisala CT25K on 3 November 2009. Data are sorted by the values of LWP from MWR. Every panel shows the corresponding value of ACI_r (Eq. 2.5) and the Pearson Product-Moment Correlation Coefficient, R , for that LWP bin.

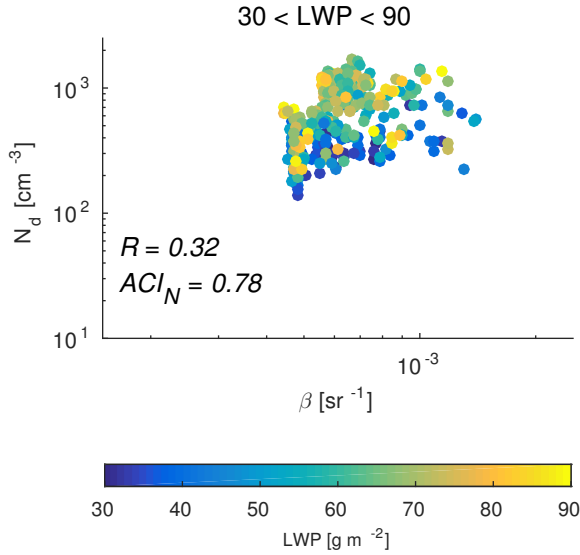


Figure 2.4: The cloud droplet number concentration N_d derived from WACR and MWR measurements with Eq. (2.11) is plotted versus the integrated attenuated backscatter ATB measured by Vaisala CT25K on 3 November 2009. Corresponding value of ACI_N (Eq. 2.7) and the Pearson Product-Moment Correlation Coefficient, R , is presented.

standard deviation of 380 cm^{-3} and mean value of 750 cm^{-3} . Values of r_e range between $2.5 \mu\text{m}$ and $7 \mu\text{m}$, with a mean radius $4.6 \mu\text{m}$ and a standard deviation of $0.65 \mu\text{m}$. ATB in the selected period has a mean value of $1.53 \times 10^{-3} \text{ sr}^{-1}$ and a standard deviation of $0.25 \times 10^{-3} \text{ sr}^{-1}$. It should be noted that on 29 November ATB is higher, but, even accounting for the uncertainty of ATB , the variation is smaller than on 3 November.

Suitable data from 29 November 2009 are divided into bins based on the value of the LWP which ranges from 30 to 90 g m^{-2} . Data was divided into 6 separate bins, each covering 10 g m^{-2} . Figure 2.7 presents relation between the integrated attenuated backscatter ATB and cloud droplet effective radius r_e together with the correlation coefficient, R and ACI_r calculated for each bin. It can be observed that data points are less scattered on the 29 November than on the 3 November and the values of both R and ACI_r are also higher. Similar to the case from the 3 November, R and ACI_r are highest in the LWP range between 40 to 70 g m^{-2} .

Figure 2.8 presents the relation between the integrated attenuated backscatter, ATB , and the cloud droplet number concentration, N_d , together with the corresponding R and ACI_N .

2.4.3. Comparison of example study cases

Table 2.3 summarises statistical parameters, including the number of observations within each LWP bin, for both study cases presented here. Values of the correlation coefficient r are generally higher for the value of LWP in the range from

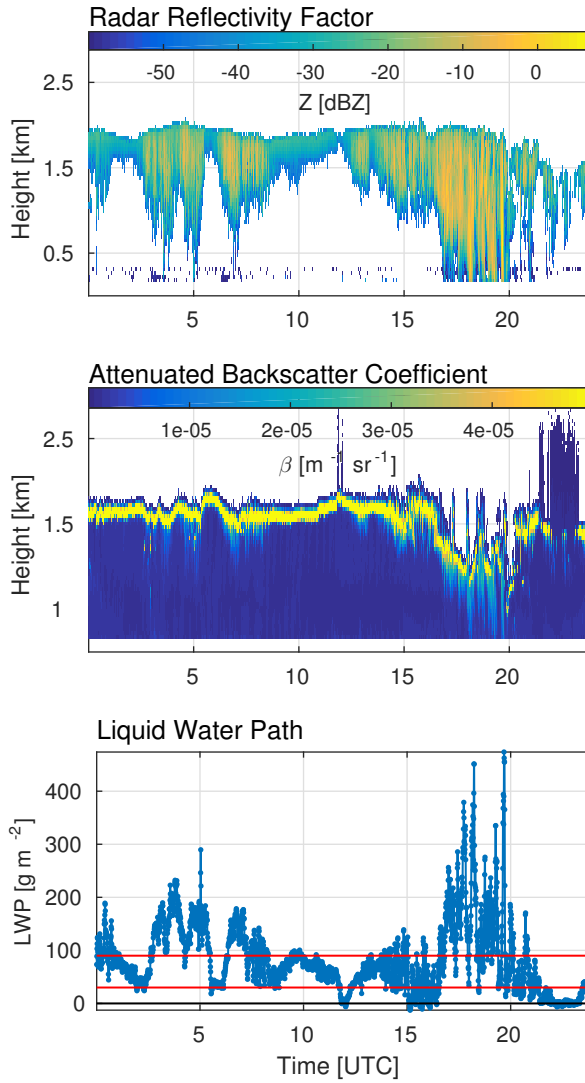


Figure 2.5: The time-height cross section of the Radar Reflectivity from WACR, the Attenuated Backscatter Coefficient from Vaisala CT25K and the Liquid Water Path from MWR for a full day of measurements on 29 November 2009.

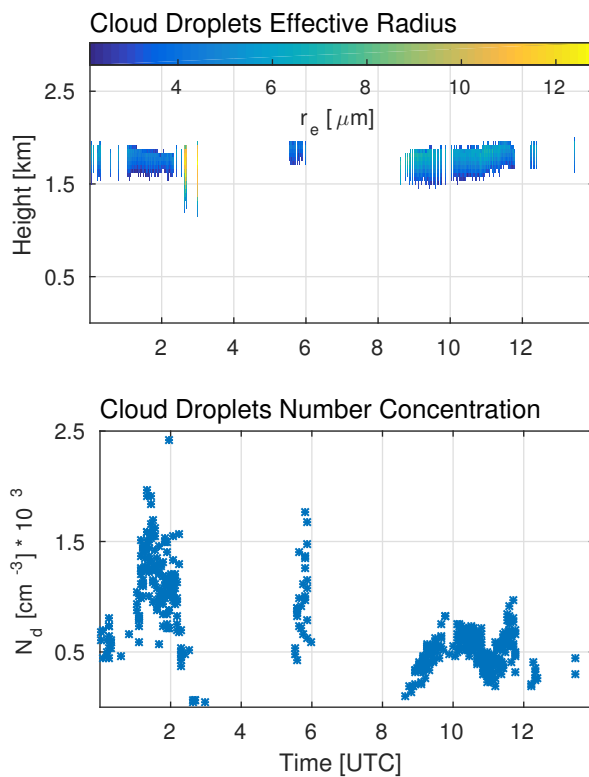


Figure 2.6: The time-height cross section of the Cloud Droplet Effective Radius (r_e) derived from the WACR and MWR (Eq. (2.10)) and the Cloud Droplet Number Concentration (N_d) calculated from Eq. (2.11) from 29 November 2009. Data are only retrieved in the time steps when the data selection criteria are met.

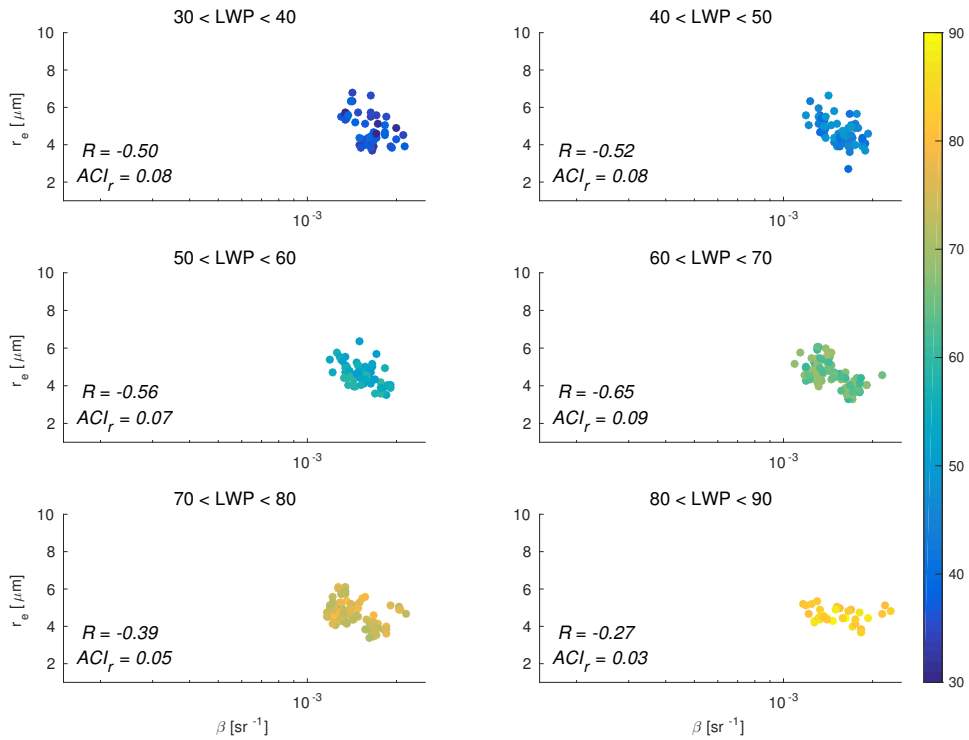


Figure 2.7: The values of the effective radius r_e derived from WACR and MWR measurements are plotted versus the integrated attenuated backscatter ATB measured by Vaisala CT25K on 29 November 2009. Data are sorted by the values of LWP from MWR. Every panel shows the corresponding value of ACI_r (Eq. 2.5) and the Pearson Product-Moment Correlation Coefficient, R , for that LWP bin.

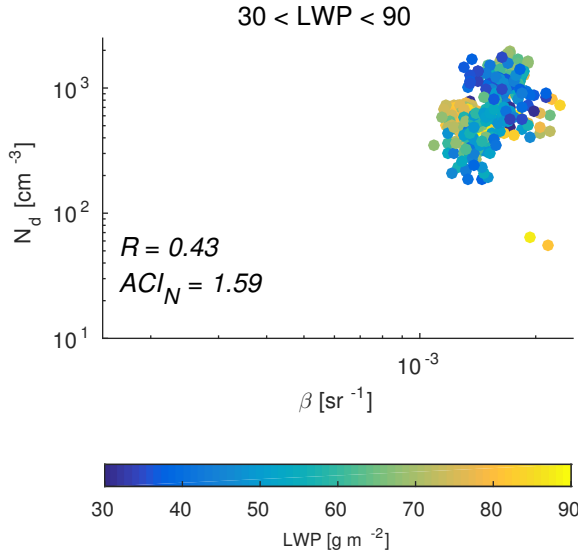


Figure 2.8: The cloud droplet number concentration N_d derived from WACR and MWR measurements with Eq. (2.11) is plotted versus the integrated attenuated backscatter ATB measured by Vaisala CT25K on 29 November 2009. Corresponding value of ACI_N (Eq. 2.7) and the Pearson Product-Moment Correlation Coefficient, R , is presented.

Table 2.3: ACI_N (Eq. 2.7) and the statistical parameters calculated between $\ln(N_d)$ and $\ln(ATB)$, namely the Pearson-Product Moment Correlation Coefficient, R , and the Coefficient of Determination, r^2 and the number of observations, n , for two study cases from Graciosa Island at the Azores (3 and 29 November 2009).

3 November 2009				29 November 2009			
ACI_N	R	r^2	n	ACI_N	R	r^2	n
0.78	0.32	0.10	320	1.59	0.43	0.19	408

40 to 70 gm^{-2} . This suggests that aerosol-cloud interactions connected to the droplet activation play a more important role in the lower values of LWP and that supposedly drizzle can obscure the process of the activation of aerosols into cloud droplets. For both cases the calculated values of ACI_N are very high, with the value on the 29 November of 1.59, which is exceeding the theoretical bounds (from 0 to 1).

This is possibly due to an overestimation of the cloud droplet number concentration (N_d) by the retrieval. As we mentioned before, the observational values of N_d for marine Stratocumulus clouds are around 200–300 cm^{-3} and the retrieved values for both presented here study cases exceed this range drastically. Therefore, we think that it's more reasonable to compare the values of ACI_r , which are between 0 and 0.09 in this study. This range of ACI_r is comparable to other studies of aerosol-cloud interactions performed with ground-based remote sensing instruments (for example, reported values range from 0.04 to 0.15 in McComiskey *et al.* [8]).

2.5. Summary and Outlook

In this paper we present a method for observing aerosol-cloud interactions. This method enables continuous monitoring of cloud microphysical responses to the changing aerosols concentration. It utilizes high resolution ground-based remote sensing instruments. This scheme uses standardised data streams from Cloudnet as input. Therefore this method can be applied at any ground-based cloud observatory participating in the Cloudnet network. We used the Cloudnet cloud categorisation product to choose data points with the specific targets only (liquid water clouds and aerosol). Instead of aggregating data with same values of LWP over a longer period we process data from every day separately.

Daily data for analysis is selected based on a range of criteria. Data points complying with all of them are divided into bins of LWP where each bin is 10 gm^{-2} wide. For every bin we calculate the Pearson-Product Moment Correlation Coefficient, R , ACI_r (Eq. 2.5) and the Coefficient of Determination, r^2 . We show that both the statistical parameters and ACI_r can be used to quantify the dependence of the cloud droplet size on the aerosols concentration. We showed that it is possible to derive ACI_r and the statistical parameters on a daily basis and with that ensure that no big variation in the meteorological conditions is present. Collocation of daily data into larger data sets can be made, but should be based on very similar meteorological conditions. In our study we identified similar meteorological conditions based on the temperature, pressure and specific humidity. We say that the conditions are similar if the standard deviation of each parameter is less than 10% of its mean value.

We showed two example case studies to present this method. Both data sets come from the deployment of the Atmospheric Radiation Measurement Program (ARM) Mobile Facility at Graciosa Island, Azores in 2009 and 2010. The presented cases both are characterised by a marine Stratocumulus clouds, both come from November and have similar general meteorological conditions. We show the correlation coefficient, ACI_r and the coefficient of determination for both case and all the LWP bin. We observe a higher correlation of aerosols concentration and cloud properties in the lower values of LWP (from 40 to 70 gm^{-2}). This suggests that aerosol-cloud interactions are a more significant process at values of LWP below about 70 gm^{-2} while for larger values other processes such as collision and coalescence are a dominant cloud microphysical process for the presented here study cases. A study based on a bigger data set should be performed to draw more general conclusions. We also observed an increase of the correlation between the aerosols and cloud properties when the parameters are compared at a set height dependent on the cloud base height.

The method we developed is based on a synergy of widely available, high resolution ground-based remote sensing instruments. It enables monitoring the interactions of aerosols and clouds. Although data need to comply with restrictive criteria, the use of a Cloudnet data format and the categorisation product makes data selection possible in close to real-time. We showed that using the integrated value of the attenuated backscatter from lidar enables the monitoring of aerosol-cloud interactions. The measurements from radar, lidar and microwave radiometer are collected

continuously and can therefore provide a continuous estimate of effects of aerosols concentration on cloud properties. This framework of measurements can be implemented at any observatory where the Cloudnet data set is available and can be integrated into a Cloudnet framework as one of the standard products. The software developed for this methodology is available under GNU General Public License [37]. Monitoring aerosol-cloud interactions in the same manner over multiple regions will allow for more studies of these phenomena and will result in a better understanding of the interactions between aerosols and clouds.

References

- [1] K. Sarna and H. W. J. Russchenberg, *Ground-based remote sensing scheme for monitoring aerosol–cloud interactions*, *Atmospheric Measurement Techniques* **9**, 1039 (2016).
- [2] IPCC, ed., *Climate Change 2013 - The Physical Science Basis: Working Group I Contribution to the Fifth Assessment Report of the Intergovernmental Panel on Climate Change* (Cambridge University Press, Cambridge, 2014).
- [3] S. Twomey, *Pollution and the planetary albedo*, *Atmos. Environ.* **8**, 1251 (1974).
- [4] G. Feingold, W. L. Eberhard, D. E. Veron, and M. Previdi, *First measurements of the Twomey indirect effect using ground-based remote sensors*, *Geophys. Res. Lett.* **30**, 1287 (2003).
- [5] J. Schmidt, A. Ansmann, J. Bühl, H. Baars, U. Wandinger, D. Müller, and A. V. Malinka, *Dual-FOV Raman and Doppler lidar studies of aerosol-cloud interactions: Simultaneous profiling of aerosols, warm-cloud properties, and vertical wind*, *Journal of Geophysical Research: Atmospheres* **119**, 5512 (2014).
- [6] T. J. Garrett, C. Zhao, X. Dong, G. G. Mace, and P. V. Hobbs, *Effects of varying aerosol regimes on low-level Arctic stratus*, *Geophys. Res. Lett.* **31**, L17105 (2004).
- [7] B.-G. Kim, M. A. Miller, S. E. Schwartz, Y. Liu, and Q. Min, *The role of adiabaticity in the aerosol first indirect effect*, *J. Geophys. Res.* **113**, D05210 (2008).
- [8] A. McComiskey, G. Feingold, A. S. Frisch, D. D. Turner, M. A. Miller, J. C. Chiu, Q. Min, and J. A. Ogren, *An assessment of aerosol-cloud interactions in marine stratus clouds based on surface remote sensing*, *J. Geophys. Res.* **114**, D09203 (2009).
- [9] Y. J. Kaufman, I. Koren, L. A. Remer, D. Rosenfeld, and Y. Rudich, *The effect of smoke, dust, and pollution aerosol on shallow cloud development over the Atlantic Ocean*, *PNAS* **102**, 11207 (2005).
- [10] A. McComiskey and G. Feingold, *The scale problem in quantifying aerosol indirect effects*, *Atmos. Chem. Phys.* **12**, 1031 (2012).
- [11] A. J. Illingworth, R. J. Hogan, E. J. O'Connor, D. Bouniol, J. Delanoë, J. Pelon, A. Protat, M. E. Brooks, N. Gaussiat, D. R. Wilson, D. P. Donovan, H. K. Baltink, G.-J. van Zadelhoff, J. D. Eastment, J. W. F. Goddard, C. L. Wrench, M. Haefelin, O. A. Krasnov, H. W. J. Russchenberg, J.-M. Piriou, F. Vinit, A. Seifert, A. M. Tompkins, and U. Willén, *Cloudnet*, *Bull. Amer. Meteor. Soc.* **88**, 883 (2007).
- [12] S. Twomey and J. Warner, *Comparison of Measurements of Cloud Droplets and Cloud Nuclei*, *J. Atmos. Sci.* **24**, 702 (1967).

- [13] H. R. Pruppacher and J. D. Klett, *Microphysics of Clouds and Precipitation* (Springer, 2010).
- [14] S. Twomey, *The Influence of Pollution on the Shortwave Albedo of Clouds*, *J. Atmos. Sci.* **34**, 1149 (1977).
- [15] G. L. Stephens, *Radiation Profiles in Extended Water Clouds. II: Parameterization Schemes*, *J. Atmos. Sci.* **35**, 2123 (1978).
- [16] G. Feingold, *Modeling of the first indirect effect: Analysis of measurement requirements*, *Geophys. Res. Lett.* **30**, 1997 (2003).
- [17] G. Feingold, L. A. Remer, J. Ramaprasad, and Y. J. Kaufman, *Analysis of smoke impact on clouds in Brazilian biomass burning regions: An extension of Twomey's approach*, *J. Geophys. Res.* **106**, 22907 (2001).
- [18] H. Köhler, *The nucleus in and the growth of hygroscopic droplets*, *Trans. Faraday Soc.* **32**, 1152 (1936).
- [19] D. Lamb and J. Verlinde, *Physics and Chemistry of Clouds* (Cambridge University Press, 2011).
- [20] G. M. Martin, D. W. Johnson, and A. Spice, *The Measurement and Parameterization of Effective Radius of Droplets in Warm Stratocumulus Clouds*, *J. Atmos. Sci.* **51**, 1823 (1994).
- [21] M.-L. Lu, W. C. Conant, H. H. Jonsson, V. Varutbangkul, R. C. Flagan, and J. H. Seinfeld, *The Marine Stratus/Stratocumulus Experiment (MASE): Aerosol-cloud relationships in marine stratocumulus*, *J. Geophys. Res.* **112**, D10209 (2007).
- [22] R. J. Hogan and E. J. O'Connor, *Facilitating cloud radar and lidar algorithms: the Cloudnet Instrument Synergy/Target Categorization product*, (2004).
- [23] A.-M. Sundström, T. Nousiainen, and T. Petäjä, *On the Quantitative Low-Level Aerosol Measurements Using Ceilometer-Type Lidar*, *J. Atmos. Oceanic Technol.* **26**, 2340 (2009).
- [24] M. Wiegner, F. Madonna, I. Biniotoglou, R. Forkel, J. Gasteiger, A. Geiß, G. Pappalardo, K. Schäfer, and W. Thomas, *What is the benefit of ceilometers for aerosol remote sensing? An answer from EARLINET*, *Atmos. Meas. Tech.* **7**, 1979 (2014).
- [25] C. Münkel, N. Eresmaa, J. Räsänen, and A. Karppinen, *Retrieval of mixing height and dust concentration with lidar ceilometer*, *Boundary-Layer Meteorol* **124**, 117 (2006).
- [26] V. A. Kovalev, *Solutions in LIDAR Profiling of the Atmosphere* (John Wiley & Sons, 2015).

- [27] J. Schmidt, A. Ansmann, J. Bühl, and U. Wandinger, *Strong aerosol–cloud interaction in altocumulus during updraft periods: lidar observations over central Europe*, *Atmospheric Chemistry and Physics* **15**, 10687 (2015).
- [28] G. Feingold, R. Furrer, P. Pilewskie, L. A. Remer, Q. Min, and H. Jonsson, *Aerosol indirect effect studies at Southern Great Plains during the May 2003 Intensive Operations Period*, *J. Geophys. Res.* **111**, D05S14 (2006).
- [29] E. J. O'Connor, A. J. Illingworth, and R. J. Hogan, *A Technique for Autocalibration of Cloud Lidar*, *J. Atmos. Oceanic Technol.* **21**, 777 (2004).
- [30] S. Frisch, M. Shupe, I. Djalalova, G. Feingold, and M. Poellot, *The Retrieval of Stratus Cloud Droplet Effective Radius with Cloud Radars*, *J. Atmos. Oceanic Technol.* **19**, 835 (2002).
- [31] C. L. Knist, *Retrieval of liquid water cloud properties from ground-based remote sensing observations*, Ph.D. thesis, TU Delft: Civil Engineering and Geosciences: Geoscience and Remote Sensing (2014).
- [32] J.-L. Brenguier, F. Burnet, and O. Geoffroy, *Cloud optical thickness and liquid water path – does the k coefficient vary with droplet concentration?* *Atmos. Chem. Phys.* **11**, 9771 (2011).
- [33] D. D. Turner, A. M. Vogelmann, K. Johnson, M. Miller, R. T. Austin, J. C. Barnard, C. Flynn, C. Long, S. A. McFarlane, K. Cady-Pereira, S. A. Clough, J. C. Chiu, M. M. Khaiyer, J. Liljegren, B. Lin, P. Minnis, A. Marshak, S. Y. Matrosov, Q. Min, W. O'Hirok, Z. Wang, and W. Wiscombe, *Thin Liquid Water Clouds: Their Importance and Our Challenge*, *Bull. Amer. Meteor. Soc.* **88**, 177 (2007).
- [34] J. Rémillard, P. Kollias, E. Luke, and R. Wood, *Marine Boundary Layer Cloud Observations in the Azores*, *J. Climate* **25**, 7381 (2012).
- [35] J. B. M. Widener, K. B., *W-Band ARM cloud radar–Specifications and design*, in *Fourteenth ARM Science Team Meeting Proceedings* (Albuquerque, New Mexico, 2004).
- [36] R. R. Draxler, A. R. L. (U.S.), and G. D. Hess, *Description of the HYSPLIT-4 Modeling System* (National Oceanic and Atmospheric Administration, 1997).
- [37] K. Sarna, *ACI monitoring: First release*, (2015).

3

Monitoring Aerosol–Cloud Interactions at the CESAR Observatory in the Netherlands

Karolina Sarna, H.W.J. Russchenberg

The representation of aerosol–cloud interactions (ACI) processes in climate models, although long studied, still remains the source of high uncertainty. Very often there is a mismatch between the scale of observations used for ACI quantification and the ACI process itself. This can be mitigated by using observations from ground-based remote sensing instruments. In this paper we presented a direct application of the Aerosol–Cloud Interactions monitoring technique (ACI monitoring). ACI monitoring is based on the standardized Cloudnet data stream, which provides measurements from ground-based remote sensing instruments working in synergy. For the dataset collected at the CESAR Observatory in the Netherlands we calculate ACI metrics. We use specifically attenuated backscatter coefficient (ATB) for the characterisation of the aerosols properties and cloud droplet effective radius (r_e) and number concentration (N_d) for the characterisation of the cloud properties. We calculate two metrics: $ACI_r = \ln(r_e)/\ln(ATB)$ and $ACI_N = \ln(N_d)/\ln(ATB)$. The calculated values of ACI_r range from 0.001 to 0.085, which corresponds to the values reported in previous studies. We also evaluated the impact of the

This chapter has been published in Atmospheric Measurement Techniques **10**, 1987–1997, 2017 [1].

vertical Doppler velocity and liquid water path (LWP) on ACI metrics. The values of ACI_r were highest for LWP values between 60 and 105 gm^{-2} . For higher LWP other processes, such as collision and coalescence, seem to be dominant and obscure the ACI processes. We also saw that the values of ACI_r are higher when only data points located in the updraft regime are considered. The method presented in this study enables monitoring ACI daily and further aggregating daily data into bigger datasets.

3.1. Introduction

Clouds are one of the most important systems of regulating Earth's radiation. Through changes in their macro- and microphysical properties clouds can significantly affect climate [2]. Aerosols and their ability to act as cloud condensation nuclei can alter cloud microphysical properties. Twomey [3] was the first one to postulate that the increasing pollution, represented by aerosols concentration, leads to an increasing cloud droplet concentration and a decreasing cloud droplet size. The effect of those microphysical changes is an increased albedo of clouds. Despite the good understanding of the physical principles of the aerosol–cloud interactions (ACI) processes, their representation in the climate models remains the source of the highest uncertainty [4].

The conceptual process in which aerosols become activated into cloud droplet is well understood [5]. Also, the influence of the aerosols concentration on the cloud microphysical properties, i.e. cloud droplet size and number concentration, has been studied extensively over the past decades [6–9] and its existence is not in question. The biggest uncertainty still lies with the scale of the process and its importance over different locations and in different meteorological conditions. Another sources of uncertainty is connected to disentangling effects of ACI on cloud properties from the effect of cloud thermodynamics and entrainment [10]. Mccomiskey *et al.* [11] identified the mismatch in the scale of the ACI process and in the scale of the observations as one of the largest drivers of uncertainty in quantifying ACI. One possible way of overcoming this problem is by using the observations from ground-based remote sensing instruments. Ground-based remote sensing instruments are uniquely predisposed to provide high temporal resolution of measurements continuously. At the same time, they can examine the effect of change in aerosols concentration on cloud in a single air column and at the scale of the cloud droplet formation. Ground based remote sensing instruments are operating at a high temporal and spatial resolution. Hence, it is possible to measure aerosols properties with a ground-based lidar with a high accuracy [12] and the same is true for cloud droplet observation with the use of cloud radar and radiometer [13].

In the past years several studies used measurements from ground-based remote sensing instruments to quantify ACI [e.g., 6, 14–16]. The scope of instruments and measured parameters still differs among them. Further, a great majority of ACI studies is focused on the marine or coastal environment. Although harder to observe, ACI over continents is important to make a link between anthropogenic aerosols and the radiative forcing through the ACI process.

A new approach to monitor ACI based on a standardized data format was proposed by [17]. Their method (hereafter referred to as ACI monitoring) is based on the Cloudnet data [18], a unified data format that is available across the Cloudnet network observatories. ACI monitoring also supplied an open-source software [19] to process data from any Cloudnet station. In this paper we applied this method directly to the dataset from the CESAR (Cabauw Experimental Site for Atmospheric Research) Observatory.

The structure of this paper is following: first we present shortly the theoretical framework for calculations, secondly we provide a description of the CESAR Obser-

vatory and the used dataset. Then we characterize ACI over the CESAR Observatory and describe different drivers of the ACI process at this station. We finish with a summary and conclusions.

3.2. Theoretical basis of aerosol–cloud interactions

The relation between aerosols concentrations and the cloud droplet size was first postulated by [3]. Using airborne measurements he showed that an increasing pollution, and hence an increasing concentration of CCN, will result in clouds with a higher optical thickness. That is measurable only if all other parameters, mainly the amount of available water represented by the liquid water path (LWP), are kept the same. Cloud optical thickness can be related to both the cloud albedo and cloud microphysical properties. Cloud optical thickness (τ_d) is proportional to the cloud droplet number concentration (N_d):

$$\tau_d \propto N_d^{1/3} \quad (3.1)$$

[20].

Proxies used to define the aerosols background vary between studies and include parameters such as: aerosols number concentration (N_a), aerosols optical thickness (τ_a), or aerosol index. The relation between N_d and N_a was postulated first based on the experimental studies by Twomey *et al.*[21] as

$$N_d \propto N_a^\gamma, \quad (3.2)$$

where γ is a factor with which aerosols number concentration and cloud droplet number concentration depend on each other. The theoretical values of γ vary between 0 and 1. To account for γ , [6] introduced the indirect effect index, which hereafter will be referred to as ACI metric. It was defined as a relative change in the cloud properties due to changes in the aerosols properties. Based on the relation in Eq. 3.2 we can say that:

$$ACI_N = \frac{d \ln N_d}{d \ln \alpha}, \quad 0 < ACI_N < 1, \quad (3.3)$$

where α is any of the above mentioned proxies of the aerosols properties. The value of ACI_N can be related to the value of γ . To relate aerosols properties to cloud droplet size [6] used:

$$ACI_r = - \left. \frac{d \ln r_e}{d \ln \alpha} \right|_{LWP}, \quad 0 < ACI_r < 0.33, \quad (3.4)$$

where r_e is the cloud droplet effective radius in the cloud base region. Cloud base area is defined as the range between the cloud base and 30 meters above the cloud base. The bounds of ACI_r between 0 and 0.33 stem from the assumption of a constant LWP when using r_e . ACI_N is traditionally not bound by the values of LWP as it is associated with the activation process which has no direct microphysical relation to LWP [9]. The relation between ACI_r and ACI_N is described as:

$$ACI_r = \frac{1}{3} ACI_N. \quad (3.5)$$

Mathematically, both ACI_r and ACI_N are defined as a slope of the regression line between the logarithm of the aerosols property (α) and the logarithm of the cloud property (r_e or N_d). For this explanation we use r_e as a cloud property. We can define a linear regression between $\ln(\alpha)$ and $\ln(r_e)$ as:

$$\ln(r_e) = a + m * \ln(\alpha) \quad (3.6)$$

where m is the slope defined as:

$$m = r_{\alpha, r_e} \frac{s_{r_e}}{s_{\alpha}}, \quad (3.7)$$

where r_{α, r_e} is the Pearson product-moment correlation coefficient between $\ln(\alpha)$ and $\ln(r_e)$, s_{r_e} is the standard deviation of $\ln(r_e)$ and s_{α} is the standard deviation of $\ln(\alpha)$. The correlations coefficient r_{α, r_e} is defined as:

$$r_{\alpha, r_e} = \frac{cov(\alpha, r_e)}{s_{\alpha} s_{r_e}}. \quad (3.8)$$

$cov(\alpha, r_e)$ is the covariance between $\ln(\alpha)$ and $\ln(r_e)$. In this study we use ACI monitoring scheme which relies both on the calculation of the correlation coefficient and ACI metrics (ACI_N and ACI_r).

3.3. Methodology of an ACI monitoring scheme

As we mentioned in previous sections, in this paper we use the Aerosol–Cloud Interaction (ACI) monitoring scheme as described in [17]. The core of this method is the Cloudnet dataset. It provides a standardized data stream from ground-based remote sensing instruments working in synergy. In specific, it includes measurements from cloud radar, lidar and microwave radiometer. Although this is a set of instruments present at all observatories within the Cloudnet network, their specification may vary from station to station.

Cloudnet dataset was designed to facilitate the retrieval of microphysical cloud properties. Therefore, a retrieved values of cloud droplet effective radius (r_e) and cloud droplet number concentration (N_d) are available from the dataset. The microphysical retrieval method used in the Cloudnet dataset is based on the method designed by [22]. In this paper we use the [22] retrieval with the assumptions of homogeneous mixing as described in [13]. The aerosols background is represented in the ACI monitoring scheme by an integrated value of the attenuated backscatter coefficient (ATB). The value is integrated from the height of a complete overlap [23], which is 120 m in the setup of this study, to 300 m below the cloud base. Measurements of ATB in the area closer to the cloud base than 300 m are not always reliable and should not be used as an approximation of the aerosols number concentration.

3.3.1. Data selection criteria

Due to the use of cloud microphysical properties the ACI monitoring scheme is applicable only under specific conditions. In particular, only low-level liquid water clouds in well-mixed conditions can be considered. We define the well-mixed condition as a cloud at the top of the boundary layer, where the vertical mixing of the layer is strong. The cloud base should be located below 2000 m above ground level (AGL). This constraint was chosen as the cloud base of the Stratocumulus clouds is usually situated below 2000 m AGL. Due to the integrations of *ATB* only clouds with cloud base located above 500 m AGL are considered. This is because the complete overlap is at 120 m and data is only considered up to 300 m below the cloud. *ATB* should be integrated through at least 2 range gates of the used lidar, which for most Cloudnet observatories are 40 m wide. Further filtering criteria include presence of precipitation or drizzle. The Cloudnet dataset contains target classification where liquid cloud droplets are categorized specifically [24]. ACI monitoring scheme selects only data points where liquid cloud droplets and aerosols are identified. All other data points are disregarded, i.e. all points where any form of precipitation or insects were identified by the Cloudnet classification scheme.

For the dataset used in this study we aggregated daily data into one dataset. The data aggregation is only possible if data was collected in similar meteorological conditions. We define the meteorological conditions on the basis of temperature and pressure at the cloud base level. We considered conditions to be similar if the relative standard deviation (rsd) of the measurements is less than 0.1. The relative standard deviation is defined as a ratio of the standard deviation of the dataset to the mean of the dataset. As an additional meteorological parameter we use specific humidity. However, the changes in the specific humidity can be larger than those in temperature or pressure. The condition of the constant amount of available water is controlled by the liquid water path (*LWP*), which represents the total amount of liquid water in the column. It should be noted that meteorological conditions available in the Cloudnet dataset come from the KNMI (Koninklijk Nederlands Meteorologisch Instituut) regional atmospheric climate model RACMO [25] and not from the observations.

3.4. Observations from CESAR Observatory

The CESAR (Cabauw Experimental Site for Atmospheric Research) Observatory is located in the Netherlands (51.971° N, 4.927° E) in an area located 0.7 m below the mean sea level. The site is equipped with a large set of instruments providing constant measurements to study atmospheric processes. The dataset used in this study was collected in October - November 2014 during the ACCEPT (Analysis of the Composition of mixed-phase Clouds with Extended Polarization Techniques) campaign. Although the ACCEPT campaign was focused on mixed-phase clouds, multiple measurements of low-level liquid water clouds were also collected. During the six weeks period of the campaign seven days were represented by a persisting layer of Stratocumulus clouds. Due to the requirements of the ACI monitoring scheme, after applying data selection criteria (see Section 3.3.1) only four days of data were processed. The total amount of measurements profiles used in this study

Table 3.1: Cloud and aerosols properties measured or derived from the observations at the CESAR Observatory in the Netherlands.

Measured Quantity	Definition	Instrument(s)
Cloud Liquid Water Path	LWP (gm^{-2})	HATPRO MWR
Radar Reflectivity Factor	Z (dBZ or $\text{m}^6 \text{m}^{-3}$)	MIRA
Doppler Velocity	w (m s^{-1})	MIRA
Cloud Droplet Effective Radius	r_e ($\square\text{m}$) [13]	MIRA/HATPRO MWR
Cloud Droplet Number Concentration	N_d (cm^{-3}) [13]	MIRA/HATPRO MWR
Attenuated Backscatter Coefficient	ATB [$\text{m}^{-1}\text{sr}^{-1}$]	CHM15X ceilometer

is 1659. We used one additional requirement to choose them: we only processed profiles where the Stratocumulus layer was persisting for at least 30 minutes. This meant that we only chose data where at least 60 profiles of 30 sec integrated measurements were consecutive. We chose to add this selection criteria to eliminate from the aggregated dataset days where only a couple of profiles responding to all selection criteria were available. This restriction was applied to avoid profiles that were only temporally fulfilling all the selection criteria of this method and in itself might have been part of a more turbid conditions.

3.4.1. Instrumentation

One of the main objectives of the ACI monitoring scheme was to develop a method that can be easily applied at various observatories. To achieve that it was necessary to base this method on a widely spread set of instruments. Those instruments include cloud radar, lidar and microwave radiometer. In this study we used specifically data from: (1) a Ka-band 35.5 GHz cloud radar MIRA, (2) a CHM15X ceilometer operating at 1064 nm and (3) HATPRO (Humidity and Temperature Profiler) microwave radiometer (MWR) operating at 14 frequencies - 7 frequencies between 22 and 31 GHz (K-band) and 7 frequencies between 51 and 58 GHz (V-Band). Data from the cloud radar MIRA and the HATPRO MWR is used for the retrieval of cloud microphysical properties, specifically cloud droplet effective radius r_e and cloud droplet number concentration N_d . Both microphysical parameters are retrieved in accordance with [13]. Data is re-sampled to an uniform time-height resolution. Time resolution is 30 seconds and height resolution (range gate) is 31.2 meters.

Moreover, cloud radar MIRA measures the Doppler velocity, which is used to measure updraft within the cloud. Data from HATPRO MWR is also used to measure liquid water path (LWP), which is used to divide data into bins. This division is made in order to consider data in conditions approaching constant amount of water available. In principle the size of LWP bins should be as small as possible. In order to have a representable data sample we make each bin 15 gm^{-2} wide. Finally, data from CHM15X ceilometer is used to measure a proxy of the aerosols concentration (i.e. the integrated value of the attenuated backscatter coefficient (ATB) [17]). Table 3.1 summarises all relevant parameters and the instruments that were used to measure and/or retrieve them. Figure 3.1 presents the distribution of all measured

quantities used in this study.

We use an additional measurement from cloud radar, the Doppler velocity, to measure updraft and downdraft. The ACI metrics are expected to be stronger in the updraft areas as that's where aerosols is activated into cloud droplets. Figure 3.2 presents the histogram of Doppler velocity in the aggregated dataset. Note that we use the average of Doppler velocity from the cloud base to two gate ranges within the cloud.

3

3.4.2. Aerosols background at CESAR

A limited amount of studies of ACI processes were focused until now on the continental low-level liquid water clouds [e.g., 6, 26]. Most studies were focused on marine or coastal liquid water clouds [e.g., 7, 9, 15]. The CESAR Observatory is located in the western part of the Netherlands. The liquid water clouds observed over CESAR have characteristics of continental clouds. Further, the aerosols background is typically continental. Aerosols over CESAR are mainly represented by a organic aerosols as well as high concentration of ammonium nitrate [27]. This type of aerosols background is important to study as it can be directly related to the anthropogenic emissions [28].

3.4.3. Selected dataset

As we mentioned in the previous sections, due to the microphysical scale of the ACI processes data need to be aggregated only under similar meteorological conditions (as defined in Section 3.3.1). This is to make sure that ACI processes are not obscured by other meteorological processes. Figure 3.3 presents histograms of the meteorological conditions of the aggregated dataset. The values of pressure and temperature show small variation, represented by a small value of the relative standard deviation (rsd), 0.03 for pressure and 0.01 for temperature. The variation of specific humidity is larger, with rsd of 0.22. To secure that the amount of available water is constant, we divide data into bins of *LWP*. It is important to note that for the Cloudnet dataset meteorological conditions are provided by the KNMI Regional Atmospheric Climate Model (RACMO) [25].

3.5. Results and discussion

3.5.1. ACI metrics

ACI metrics are representing the response of cloud microphysical properties (r_e and N_d) to aerosols properties (aerosols concentration is represented by *ATB*). To accurately quantify ACI the amount of available water should be kept constant. To meet this requirement we divide data into bins of *LWP*. Each *LWP* bin is 15 gm^{-2} wide. Calculations are made for the bins between 30 and 150 gm^{-2} . The lower limit of the *LWP* analysis range was chosen as twice the typical uncertainty of the HATPRO MWR measurements (15 gm^{-2}). The upper limit is the approximate precipitation threshold [9]. For every *LWP* bin we also calculate the Pearson product-moment correlation coefficient, r (Eq. 3.8).

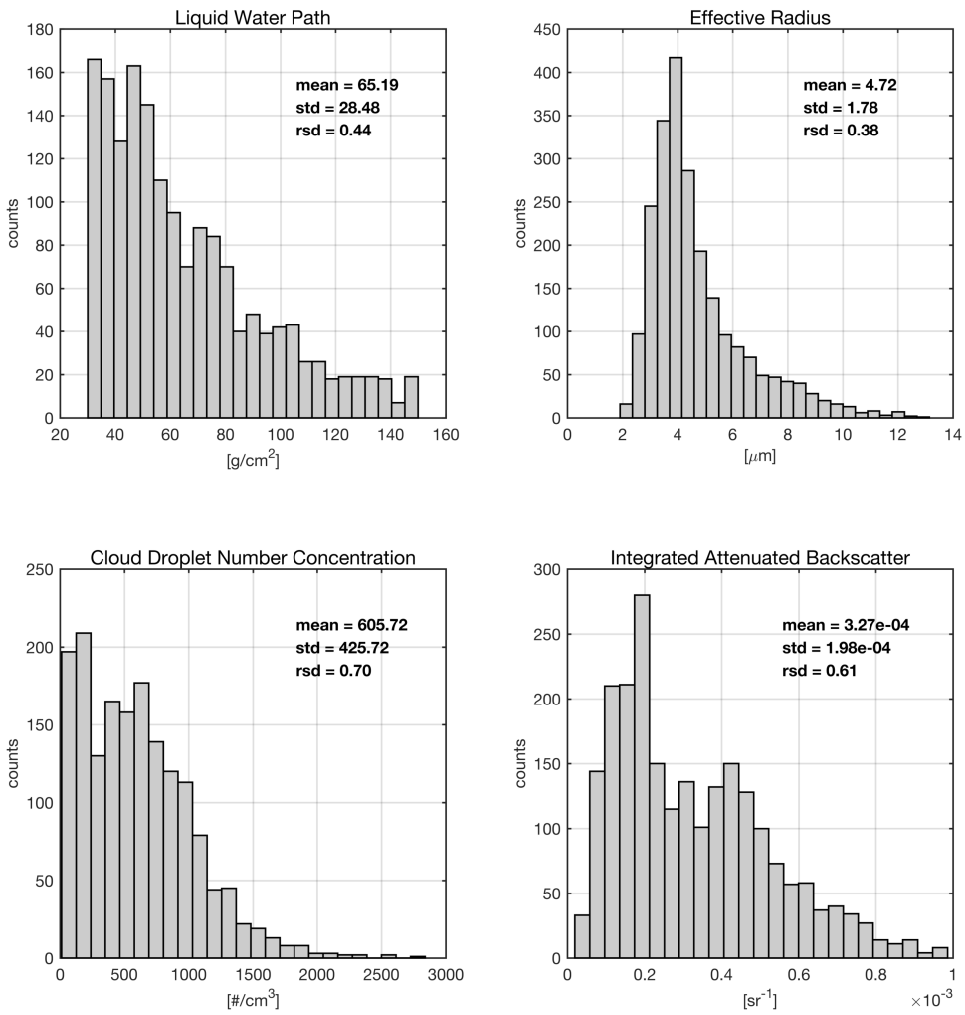


Figure 3.1: Histograms of the measurements and retrievals for the aggregated dataset.

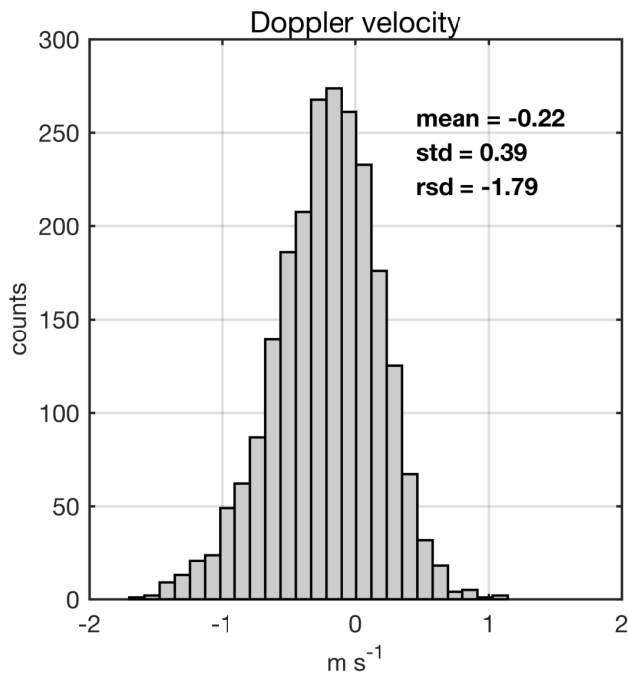


Figure 3.2: Histograms of the Doppler velocity for the aggregated dataset.

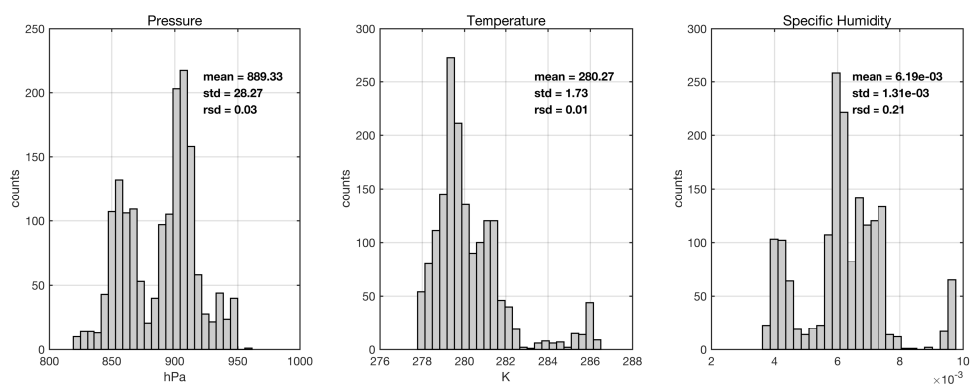


Figure 3.3: Histograms of the meteorological data for the aggregated dataset.

Table 3.2: ACI_r (Eq. 3.4) together with Pearson product-moment correlation coefficient, r , calculated between $\ln(r_e)$ and $\ln(ATB)$ calculated for the aggregated dataset. Data is divided in to bins of LWP . ACI_r is calculated for the whole dataset and only for the updraft areas. The number of measurements in each bin (n) and the percentage of data available for the updraft only areas is also presented.

LWP bin	Whole dataset			Only updraft			
	ACI_r	r	n	ACI_r	r	n	%
$30 < LWP < 45$	0.016	-0.038	468	-0.078	0.204	161	34.40
$45 < LWP < 60$	-0.011	0.023	418	-0.029	0.069	133	31.82
$60 < LWP < 75$	0.065	-0.140	269	0.205	-0.373	69	25.65
$75 < LWP < 90$	0.011	-0.023	183	0.075	-0.161	48	26.23
$90 < LWP < 105$	0.085	-0.180	140	0.128	-0.375	37	26.43
$105 < LWP < 120$	0.001	-0.001	76	0.271	-0.730	15	19.74
$120 < LWP < 135$	0.046	-0.068	57	0.034	-0.066	16	28.07
$135 < LWP < 150$	-0.104	0.175	48	-0.111	0.203	13	27.08

ACI_r

To calculate ACI_r we used Eq. 3.4. Table 3.2 compares the calculated values of ACI_r and the correlation coefficient, r , for the whole dataset and for the updraft regime only. The range of values within the physical limits (between 0 and 0.33, see Section 3.2) for the whole dataset is from 0.001 to 0.085. These values are in agreement with other studies concerned with quantifying ACI_r in continental clouds. [8] reported values of ACI_r between 0.04 and 0.17 in a study over the ground-based remote sensing site at the Southern Plains in Oklahoma, USA. For the same site, [6] reported values of ACI_r between 0.02 and 0.16. The maximum value of ACI_r calculated in this study is lower than in the above mentioned studies.

In the dataset from the CESAR Observatory we can see that values of ACI_r are generally within the physical limits for the LWP values from 60 to 135 gm^{-2} . This may indicate that ACI_r is a process that is significant only for certain values of LWP . When the values of LWP are high, above 135 gm^{-2} , other processes within the cloud, such as collision and coalescence, are dominant and obscure the ACI process.

To further investigate the impact of LWP on ACI_r we selected only the profiles which were corresponding to the updraft regime. This was done based on the Doppler velocity. Firstly, it's important to note that the dataset is significantly limited when considering only the updraft regime, only 30% of the profiles in the aggregated dataset are located in the updraft regime. However, we observe a considerable increase in the value of both ACI_r and the correlation coefficient, r . Again, we can see that the values of ACI_r increase with the increasing value of LWP . ACI_r seems to be higher for the values of LWP between 60 and 135 gm^{-2} , with an exception of LWP between 75 and 90 gm^{-2} . Note that for LWP above 135 gm^{-2} values of ACI_r are exceeding the physical boundaries and indicate that the process is no longer observable. The increase of ACI_r in the updraft regime should be further investigate in a dataset with more profiles, as the reduction of the sample size is significant.

Table 3.3: ACI_N (Eq. 3.3) together with Pearson product-moment correlation coefficient, r , calculated between $\ln(N_d)$ and $\ln(ATB)$ calculated for the aggregated dataset. Data is divided in to bins of LWP . ACI_N is calculated for the whole dataset and only for the updraft areas. The number of measurements in each bin (n) and the percentage of data available for the updraft only areas is also presented.

LWP bin	Whole dataset			Only updraft			
	ACI_N	r	n	ACI_N	r	n	%
$30 < LWP < 45$	0.141	0.100	468	-0.068	-0.049	161	34.40
$45 < LWP < 60$	0.170	0.118	418	-0.009	-0.008	133	31.82
$60 < LWP < 75$	0.490	0.308	269	0.479	0.280	69	25.65
$75 < LWP < 90$	0.235	0.181	183	0.137	0.101	48	26.23
$90 < LWP < 105$	0.222	0.142	140	0.326	0.268	37	26.43
$105 < LWP < 120$	-0.034	-0.021	76	-0.084	-0.065	15	19.74
$120 < LWP < 135$	-0.269	-0.169	57	-0.149	-0.113	16	28.07
$135 < LWP < 150$	0.180	0.123	48	0.041	0.038	13	27.08

ACI_N

The response of the cloud droplet concentration to the aerosols background is an approximation of the activation process. ACI_N can be directly linked to Eq. 3.2. We calculate the relative change of N_d with the change of ATB from Eq. 3.3. For the aggregated dataset from CESAR Observatory the value of ACI_N is 0.21. The value of 0.19 is very small, often values reported in the literature vary between 0.48 and 0.99 [9, and references within]. However, it has been noted before that the size of aerosols may influence the value of ACI_N . Smaller aerosols size tends to yield smaller ACI_N [9]. Based on the aerosols background at the CESAR Observatory (see Section 3.4.2) we expect a smaller size of the aerosols particles. Another possible explanation is that values of N_d used in this study are calculated for the whole cloud and the ACI process is expected mostly in the cloud base and cloud top area. It is also important to note that the retrieval of N_d has very high estimated uncertainties, ranging between 40 and 60% [13]. Those uncertainties are mainly due to the instruments and algorithms errors and were discussed extensively in [13]. In comparison, the uncertainty of the r_e ranges between 10 and 15%. We expect that this high uncertainty is responsible for the low value of ACI_N calculated for the whole dataset.

As we mentioned above, based on the theoretical relationships between aerosols and cloud droplets ACI_N is not dependent on the LWP . However, in this study we decided to test if there is a dependence of ACI_N on the LWP by dividing data into the same bins of LWP as with the calculation of ACI_r . Table 3.3 presents the comparison of the ACI_N calculated for each LWP bin for the whole dataset and only for the updraft regime. What is striking, is that similar as in the case of ACI_r the highest values of ACI_N are present in the range between 60 and 105 gm^{-2} . We further selected only the points within the updraft regime. Again, consistently with ACI_r , the highest values of ACI_N are noted for the LWP between 60 and 75 gm^{-2} . For the values LWP above 105 gm^{-2} the increase of the value of ATB no longer corresponds to the increase of the value of N_d .

ACI_N and ACI_r are theoretically related as in Eq. 3.5. In the dataset analysed in this study this relation is not always present. We expect that the main reason for that is the discrepancy between how ACI_N and ACI_r are calculated. In particular: for the calculation of ACI_r we only use the values of r_e in the cloud base area (defined as the range between the cloud base and 30 meters into the cloud) and for the calculation of ACI_N the value of N_d is derived for the whole cloud. Another important reason might be the high uncertainty of the N_d retrieval. Also, ACI_N is harder to derive. Based on this study, we can say that ACI_r seems to give more realistic results as they are broadly in agreement with the previous studies (see Section 3.5.1).

3.5.2. Impact of updrafts

Activation of the aerosols particles into cloud droplets is invigorated in the updraft zones [29]. In this study we identified updraft areas with the use of the Doppler velocity (w). Tables 3.2 and 3.3 compare the results of ACI_r and ACI_N calculated for all *LWP* bins. Both parameters seem to indicate stronger relation between cloud properties (r_e and N_d) and aerosols properties (*ATB*) in the updraft areas. This is implicated by the increase of both the *ACI* metrics as well as the correlation coefficients. The invigoration of *ACI* processes in the updraft regime was also reported in previous studies [16]. It is important to note that the amount of available profiles is greatly diminished by the selection of updraft areas only. Specifically, the amount of profiles in the updraft regime is reduced by 70% compared to all the selected profiles. The number of samples in *LWP* bins over 105 gm^{-2} is too small to make significant conclusions. However, we can clearly observe that both ACI_r and ACI_N have the highest values in the *LWP* bins between 60 and 105 gm^{-2} .

3.5.3. Relation with *LWP*

One of the conditions for observing changes in microphysical properties of clouds due to an aerosols number concentration initially postulated by [3] was the constant amount of water available. Over the past decades different studies used that conditions with liberty. In the satellite remote-sensing quantification of *ACI* the constraint of *LWP* is often omitted [e.g., 30]. In the ground-based remote sensing methods the constraint on *LWP* is kept, but the size of *LWP* bins varies greatly. The division into *LWP* bins is important as it is still not clear if *ACI* is a significant process in different *LWP* regimes.

In this study we divided data into *LWP* bins 15 gm^{-2} wide. This was the lowest width of the bin that was allowed by the instrument restrictions (see Section 3.4.1). We saw significant changes in the calculated values of both ACI_r and ACI_N in different *LWP* bins. When the considered *LWP* bins are wider, those differences are not visible and it is difficult to define the conditions that invigorate the *ACI* processes. The drawback of applying small bins is the sample size. However, what we wanted to present with this method is the variety of values in different bins. Figure 3.4 presents the values of ACI_r plotted against *LWP* for both the whole dataset and the selected profiles in the updraft regime. We can observe an increase of ACI_r with *LWP* in the range between 60 and 105 gm^{-2} for both the updraft and the whole

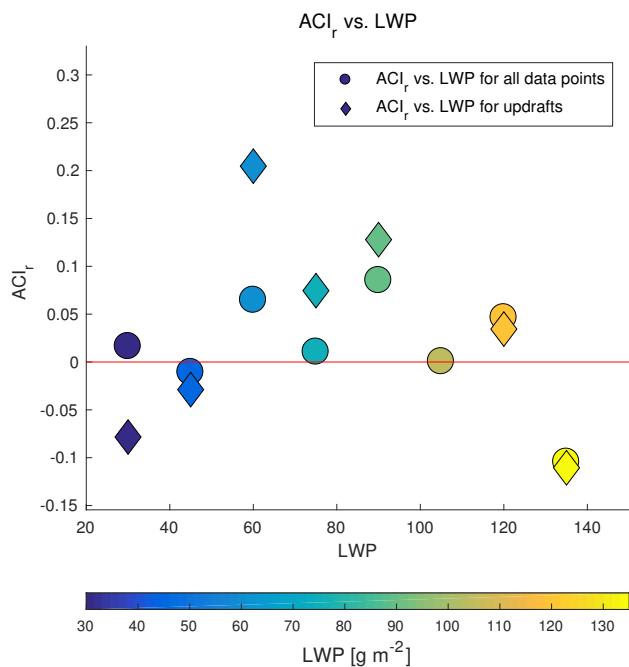


Figure 3.4: Scatter plot between ACI_r and LWP for all data points and the data points located in the updraft areas in the aggregated dataset.

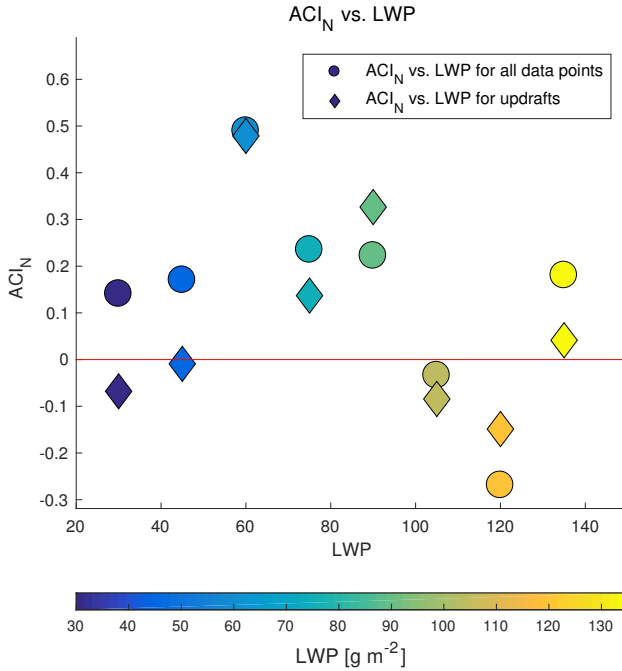


Figure 3.5: Scatter plot between ACI_N and LWP for the data points located in the updraft areas of the aggregated dataset.

dataset. What is interesting, is the negative value, and therefore outside of the physical boundaries, of the ACI_r for very small (30 to 60 $g\ m^{-2}$) and very high (135 to 150 $g\ m^{-2}$) values of LWP . This may indicate that the ACI processes are only observable in certain LWP conditions. Importantly, this is even more pronounced in the updraft regime. It should be noted that the negative values of ACI_r can also be caused by the small sample size and the errors in the retrieval of r_e . Figure 3.5 presents the values of ACI_N plotted against LWP for both the whole dataset and the selected profiles in the updraft regime. The most striking observation here is that the value of ACI_N in the updraft regime is in the majority of the LWP bins lower than in the whole dataset, unlike in the case of ACI_r where the updraft regime is related with the higher values of ACI_r in comparison to the whole dataset. The possible explanation for this phenomenon is, like we mentioned before, the difference in the calculation method: ACI_r being calculated for the cloud base region only, whereas ACI_N is calculated for the whole cloud.

3.5.4. Relation between correlation coefficient (r) and ACI_r

Most of the studies concerned with aerosol–cloud interactions calculate either ACI_r (Eq. 3.4), ACI_N (Eq. 3.3) or both to quantify the relationship between aerosols and cloud properties. As we explained before, in mathematical terms ACI_r and

ACI_N are a slope of the regression line calculated between natural logarithm of the aerosols properties and a natural logarithm of the cloud properties. The aerosols property is treated as the independent variable and the cloud property is the dependent variable. As we shown in Section 3.2, correlation coefficient and slope of the regression line are related as in Eq. 3.6.

For the dataset from the CESAR Observatory we compared the values of ACI_r with the values of the correlation coefficient. We did this comparison for every LWP bin for the whole dataset and then separately only for the profiles corresponding to the updraft area and to the downdraft area. Figure 3.6 presents the scatter plot between ACI_r and the correlation coefficient. We can observe most of the values of ACI_r that fall outside of the physical bounds are observed for the downdraft areas of the whole dataset or for the very small or very high bins of the LWP . This further underlines the impact of the updraft and LWP on the aerosol–cloud interactions. The relation between the correlation coefficient and ACI_r is mathematically sound, however, not often presented in the literature. Based on the analysed dataset we can say that the lower the value of the correlation coefficient between aerosols and cloud properties, the higher the calculated value of the ACI_r . However, this relation between the two parameters is only significant when data is sampled at a high temporal and spatial resolution and divided into bins of LWP to simulate the condition of a constant amount of available water. In case of no constraint on LWP or data with a low spatial resolution (i.e. satellite remote sensing aggregated datasets) the calculation of the correlation coefficient will become irrelevant, as the variance of the dataset will be minimized by the aggregation [11]. In case of the ACI monitoring scheme calculating both ACI_r and the correlation coefficient is relevant, as data is collected with a temporal and spatial resolution that corresponds to the scale of the aerosol–cloud interactions processes.

3.6. Summary and conclusions

In this chapter a direct application of the Aerosol–Cloud Interactions monitoring scheme was presented as described in [17]. We used a Cloudnet dataset from the CESAR Observatory in the Netherlands. Data were collected during the ACCEPT measurement campaign in October - November 2014. We aggregated daily measurements into one dataset based on the similar meteorological conditions. We only considered non-precipitating, low-level liquid water clouds. All forms of precipitation were disregarded based on the Cloudnet target categorisation. Investigated clouds had the cloud base located between 500 and 2000 m above ground level. Lastly, we only used periods when conditions corresponding to the above mentioned criteria were persisting for at least 30 minutes.

For the aggregated dataset we calculated ACI metrics using cloud droplet effective radius (r_e) following Eq. 3.4 and cloud droplet number concentration (N_d) following Eq. 3.3. The aerosols properties were represented by the integrated attenuated backscatter coefficient (ATB). For both ACI metrics we also calculate Pearson's moment correlation coefficient, r . For all the above mentioned calculations data were divided into bins of liquid water path (LWP), where every bin was 15 gm^{-2} wide. The calculated values of ACI_r were ranging from 0.001 to 0.085, which correspond

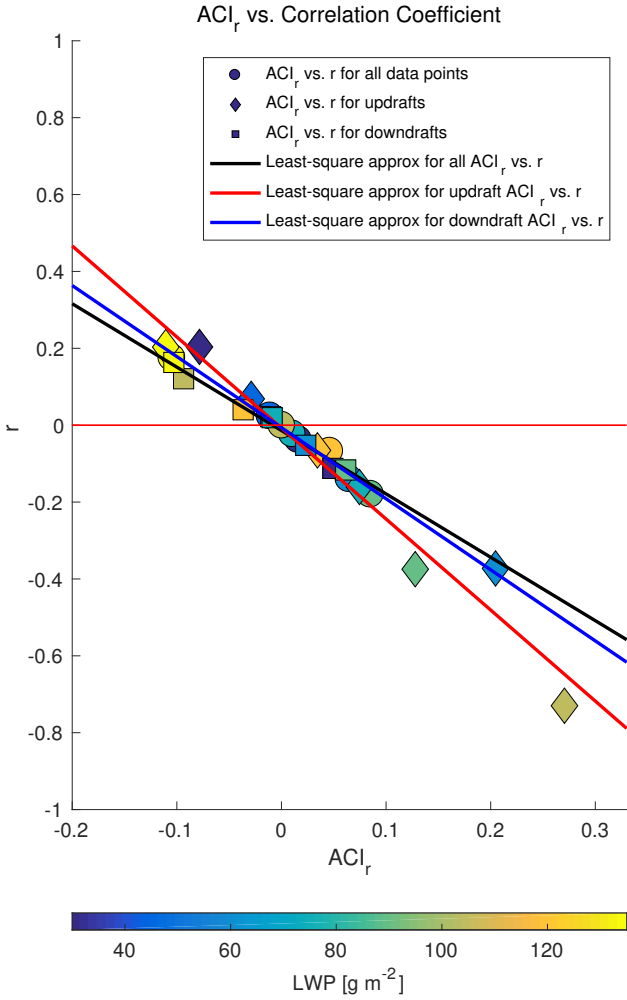


Figure 3.6: Scatter plot between ACI_r and the Pearson product-moment correlation coefficient, r.

with the values reported in the previous studies. For the low (between 30 and 60 gm^{-2}) and high (above 135 gm^{-2}) values of *LWP* we observed negative, and therefore outside of the physical bounds, values of ACI_r . This is an indication that the ACI processes are not easily observable in those *LWP* conditions and are possibly obscured by other cloud processes. The values of ACI_N were significantly lower than those reported in the literature. We attribute that to two reasons. Firstly, the retrieval of N_d is susceptible to high error, varying between 40 and 60% due to instrument errors and retrieval assumptions. Secondly, the aerosols background over the CESAR Observatory is characteristic of the continental aerosols background whereas most studies calculating ACI_N are located in the marine or coastal areas. The size of continental aerosols is significantly smaller which can lead to smaller values of ACI_N . Further, the ACI_N is calculated considering the information from the whole cloud profile, whereas ACI_r is calculated only in the cloud base area, where the ACI processes are the strongest. Considering high uncertainty of N_d retrieval, we recommend the calculation of ACI_r for accounting the impact of aerosols on the cloud microphysical properties.

We also evaluated the impact of the vertical wind speed at the cloud base and *LWP* on ACI metrics. In the analysed dataset both of those parameters showed clear impact on the values of ACI_r . The values of ACI_r were highest for the *LWP* between 60 and 105 gm^{-2} . For the higher values of *LWP* other processes, such as collision and coalescence, seem to be dominant and obscure the ACI processes. This may indicate that the approximated precipitation threshold (150 gm^{-2}) should be lowered and the Cloudnet target categorization re-evaluated. The values of ACI_r are higher when only data points located in the updraft regime were considered. As indicated in previous studies, the updraft is an important factor in invigorating aerosol–cloud interactions. The values of ACI_r in the downdraft regime were often outside of the physical bounds. It is desirable to only consider data points located within the updraft regime. However, it should be noted that selection of updraft regime only significantly decreases the data sample size.

The ACI metrics are used to account for the proportionality factor between aerosols number concentration and cloud droplet number concentration (Eq. 3.2). In this study we explained that the correlation coefficient and ACI metrics can be related for the high-resolution dataset, as ACI metrics are the slope of the regression line between cloud and aerosols properties. Therefore, a lower value of the correlation coefficient will indicate the increase of the ACI_r .

The method presented in this study enables monitoring aerosol–cloud interactions daily and further aggregating daily data into bigger datasets. We showed that it can be easily implemented at any observatory using Cloudnet data format. However, one should keep in mind that the specific conditions between the stations may vary and combining data points from various stations should be made only after assessing each one of them separately. The method describe in this paper could be implement at each station separately and then combie and compare the results from observatories with similar conditions. Such a comparison would be very valuable for a better understanding of the aerosol–cloud interactions, but was beyond the scope of this research project. A wide-spread network of ACI monitor-

ing could lead to estimating more accurately the drivers of this process in various conditions. This methodology was developed with a purpose of integration into the Cloudnet network products. Further, as the methodology presented here is based on the remote-sensing instruments only, it could be adapted to the satellite remote sensing and observation of ACI processes in the cloud top area. Such an adaptation would have to be done with care and account for all the requirements of the data selection necessary for this method.

References

- [1] K. Sarna and H. W. J. Russchenberg, *Monitoring aerosol–cloud interactions at the cesar observatory in the netherlands*, *Atmospheric Measurement Techniques* **10**, 1987 (2017).
- [2] V. Ramanathan, C. R. D., E. F. Harrison, P. Minnis, B. R. Barkstrom, E. Ahmad, and D. Hartmann, *Cloud-Radiative Forcing and Climate: Results from the Earth Radiation Budget Experiment*, *Science* **243**, 57 (1989).
- [3] S. Twomey, *The Influence of Pollution on the Shortwave Albedo of Clouds*, *J. Atmos. Sci.* **34**, 1149 (1977).
- [4] IPCC, ed., *Climate Change 2013 - The Physical Science Basis: Working Group I Contribution to the Fifth Assessment Report of the Intergovernmental Panel on Climate Change* (Cambridge University Press, Cambridge, 2014).
- [5] D. Lamb and J. Verlinde, *Physics and Chemistry of Clouds* (Cambridge University Press, 2011).
- [6] G. Feingold, W. L. Eberhard, D. E. Veron, and M. Previdi, *First measurements of the Twomey indirect effect using ground-based remote sensors*, *Geophys. Res. Lett.* **30**, 1287 (2003).
- [7] C. H. Twohy, M. D. Petters, J. R. Snider, B. Stevens, W. Tahnk, M. Wetzel, L. Russell, and F. Burnet, *Evaluation of the aerosol indirect effect in marine stratocumulus clouds: Droplet number, size, liquid water path, and radiative impact*, *J. Geophys. Res.* **110**, D08203 (2005).
- [8] B.-G. Kim, M. A. Miller, S. E. Schwartz, Y. Liu, and Q. Min, *The role of adiabaticity in the aerosol first indirect effect*, *J. Geophys. Res.* **113**, D05210 (2008).
- [9] A. McComiskey, G. Feingold, A. S. Frisch, D. D. Turner, M. A. Miller, J. C. Chiu, Q. Min, and J. A. Ogren, *An assessment of aerosol-cloud interactions in marine stratus clouds based on surface remote sensing*, *J. Geophys. Res.* **114**, D09203 (2009).
- [10] G. Feingold, A. McComiskey, T. Yamaguchi, J. S. Johnson, K. S. Carslaw, and K. S. Schmidt, *New approaches to quantifying aerosol influence on the cloud radiative effect*. *Proceedings of the National Academy of Sciences of the United States of America* , 1514035112 (2016).
- [11] A. McComiskey and G. Feingold, *The scale problem in quantifying aerosol indirect effects*, *Atmos. Chem. Phys.* **12**, 1031 (2012).
- [12] E. J. Welton, K. J. Voss, H. R. Gordon, H. Maring, A. Smirnov, B. Holben, B. Schmid, J. M. Livingston, P. B. Russell, P. A. Durkee, P. Formenti, and M. O. Andreae, *Ground-based lidar measurements of aerosols during ACE-2: instrument description, results, and comparisons with other ground-based and airborne measurements*, *Tellus B* **52**, 636 (2000).

- [13] C. L. Knist, *Retrieval of liquid water cloud properties from ground-based remote sensing observations*, Ph.D. thesis, TU Delft: Civil Engineering and Geosciences: Geoscience and Remote Sensing (2014).
- [14] T. J. Garrett, C. Zhao, X. Dong, G. G. Mace, and P. V. Hobbs, *Effects of varying aerosol regimes on low-level Arctic stratus*, *Geophys. Res. Lett.* **31**, L17105 (2004).
- [15] G. Pandithurai, T. Takamura, J. Yamaguchi, K. Miyagi, T. Takano, Y. Ishizaka, S. Dipu, and A. Shimizu, *Aerosol effect on cloud droplet size as monitored from surface-based remote sensing over East China Sea region*, *Geophysical Research Letters* **36**, L13805 (2009).
- [16] J. Schmidt, A. Ansmann, J. Bühl, and U. Wandinger, *Strong aerosol–cloud interaction in altocumulus during updraft periods: lidar observations over central Europe*, *Atmospheric Chemistry and Physics* **15**, 10687 (2015).
- [17] K. Sarna and H. W. J. Russchenberg, *Ground-based remote sensing scheme for monitoring aerosol–cloud interactions*, *Atmospheric Measurement Techniques* **9**, 1039 (2016).
- [18] A. J. Illingworth, R. J. Hogan, E. J. O’Connor, D. Bouniol, J. Delanoë, J. Pelon, A. Protat, M. E. Brooks, N. Gaussiat, D. R. Wilson, D. P. Donovan, H. K. Baltink, G.-J. van Zadelhoff, J. D. Eastment, J. W. F. Goddard, C. L. Wrench, M. Haefelin, O. A. Krasnov, H. W. J. Russchenberg, J.-M. Piriou, F. Vinit, A. Seifert, A. M. Tompkins, and U. Willén, *Cloudnet*, *Bull. Amer. Meteor. Soc.* **88**, 883 (2007).
- [19] K. Sarna, *ACI monitoring: First release*, (2015).
- [20] S. Twomey, *Pollution and the planetary albedo*, *Atmos. Environ.* **8**, 1251 (1974).
- [21] S. Twomey and J. Warner, *Comparison of Measurements of Cloud Droplets and Cloud Nuclei*, *J. Atmos. Sci.* **24**, 702 (1967).
- [22] S. Frisch, M. Shupe, I. Djalalova, G. Feingold, and M. Poellot, *The Retrieval of Stratus Cloud Droplet Effective Radius with Cloud Radars*, *J. Atmos. Oceanic Technol.* **19**, 835 (2002).
- [23] V. A. Kovalev, *Solutions in LIDAR Profiling of the Atmosphere* (John Wiley & Sons, 2015).
- [24] R. J. Hogan and E. J. O’Connor, *Facilitating cloud radar and lidar algorithms: the Cloudnet Instrument Synergy/Target Categorization product*, (2004).
- [25] E. Van Meijgaard, L. Van Uft, W. Van de Berg, F. Bosveld, B. Van den Hurk, G. Lenderink, and A. Siebesma, *The KNMI regional atmospheric climate model RACMO version 2.1* (Koninklijk Nederlands Meteorologisch Instituut, 2008).

- [26] I. Ahmad, T. Mielonen, D. P. Grosvenor, H. J. Portin, A. Arola, S. Mikkonen, T. Kühn, A. Leskinen, J. Joutsensaari, M. Komppula, K. E. J. Lehtinen, A. Laaksonen, and S. Romakkaniemi, *Long-term measurements of cloud droplet concentrations and aerosol–cloud interactions in continental boundary layer clouds*, *Tellus B* **65** (2013), 10.3402/tellusb.v65i0.20138.
- [27] A. A. Mensah, R. Holzinger, R. Otjes, A. Trimborn, T. F. Mentel, H. ten Brink, B. Henzing, and A. Kiendler-Scharr, *Aerosol chemical composition at Cabauw, The Netherlands as observed in two intensive periods in May 2008 and March 2009*, *Atmospheric Chemistry and Physics* **12**, 4723 (2012).
- [28] J.-P. Putaud, F. Raes, R. Van Dingenen, E. Brüggemann, M.-C. Facchini, S. Decesari, S. Fuzzi, R. Gehrig, C. Hüglin, P. Laj, G. Lorbeer, W. Maenhaut, N. Mihalopoulos, K. Müller, X. Querol, S. Rodriguez, J. Schneider, G. Spindler, H. ten Brink, K. Tørseth, and A. Wiedensohler, *A European aerosol phenomenology—2: chemical characteristics of particulate matter at kerbside, urban, rural and background sites in Europe*, *Atmospheric Environment* **38**, 2579 (2004).
- [29] O. Altaratz, I. Koren, L. Remer, and E. Hirsch, *Review: Cloud invigoration by aerosols—Coupling between microphysics and dynamics*, *Atmospheric Research* **140-141**, 38 (2014).
- [30] Y. J. Kaufman, I. Koren, L. A. Remer, D. Rosenfeld, and Y. Rudich, *The effect of smoke, dust, and pollution aerosol on shallow cloud development over the Atlantic Ocean*, *PNAS* **102**, 11207 (2005).

4

Estimating optical extinction of liquid water clouds in the cloud base region

Karolina Sarna, D.P. Donovan, H.W.J. Russchenberg

Accurate lidar-based measurements of cloud optical extinction, even though perhaps limited to the cloud base region, are useful. Arguably, more advanced lidar techniques (e.g. Raman) should be applied for this purpose. However, simpler polarization and backscatter lidars offer a number of practical advantages (e.g. better resolution, more continuous and numerous time series). In this paper we present a backscatter lidar signal inversion method for the retrieval of the cloud optical extinction in the cloud base region. Though a numerically stable method for inverting lidar signals using a far-end boundary value solution has been earlier demonstrated and may be considered well-established (i.e. the Klett inversion), the application to high-extinction clouds remains problematic. This is due to the inhomogeneous nature of real clouds, the finite range-resolution of many practical lidar systems and multiple-scattering effects. We use an inversion scheme where a backscatter lidar signal is inverted based on the estimated value of cloud extinction at the far end of the cloud and apply a correction for multiple-scattering within the cloud and a range resolution correction. By applying our technique to the inversion of synthetic lidar data, we show that for a retrieval of up to 90 m from the cloud base it is possible to obtain the cloud optical extinction within

This chapter has been published in Atmospheric Measurement Techniques Discussions [preprint] [1]

the cloud with an error better than 5%. In relative terms, the accuracy of the method is smaller at the cloud base but improves with the range within the cloud until 45 m and deteriorates slightly until reaching 90 m from the cloud base.

4.1. Introduction

Lidar was used to probe the atmosphere ever since 1960 [e.g., 2, 3]. Lidar measurements facilitate characterization of the atmosphere and have many different applications, including determining properties of aerosols [4] and clouds [5]. Lidars possess a unique ability to observe the optical properties of clouds such as cloud extinction coefficient (α). Through an inversion of the backscattered power received by a lidar system, an estimate of the cloud extinction coefficient can be retrieved [6]. This optical property of the cloud can be linked to cloud's microphysical properties [7]. Although lidar can only penetrate a small part of a cloud, typically 100 to 300 meters from the cloud base, the cloud base region is of a strong interest for studies concerned with cloud formation and aerosol-cloud interactions [8]. Despite the long history of lidar measurements and the vast amount of data available, very few quantitative evaluations of the cloud optical extinction retrieval accuracy under realistic conditions exist [e.g., 9, 10]. Lidar signal inversion in realistic conditions is more difficult due to the effects of finite lidar range resolution and multiple-scattering occurring within the cloud.

In this paper we present a procedure to retrieve the cloud optical extinction coefficient, using a single field of view (FOV) depolarization lidar. We use the Klett solution [6] with the inclusion of a multiple-scattering correction [11, 12] and an explicit treatment of the molecular and cloud contributions to the returned signal [13]. We demonstrate, using synthetic lidar signals generated using a Monte-Carlo RT model fed with Large-Eddy simulation (LES) fields, that useful extinction profiles can be retrieved using simple elastic polarization lidars.

The outline of the paper is as follows. In Sect. 4.2 we present background material. In Sect. 4.3 we give a brief description of the EarthCARE Simulator (ECSIM) and scenes created for this investigation. Sect. 4.4 presents the results of the inversion and discusses the issues related to conducting accurate inversions and present our methodology to address them. We conclude the paper with a summary of the findings and an outlook of possible applications.

4.2. Lidar signal inversion

The single-scattering lidar equation for a two-components atmosphere (cloud and molecular) can be defined as

$$P(z) = \frac{C_{lid}}{z^2} (\beta_{c,\pi}(z) + \beta_{m,\pi}(z)) e^{-2 \int_0^z (\alpha_c(z') + \alpha_m(z')) dz'}, \quad (4.1)$$

where z is the altitude, $P(z)$ is the received power as a function of altitude, C_{lid} is the lidar calibration constant, β_π is the atmospheric backscatter coefficient, α is the atmospheric extinction coefficient and the 'c' and 'm' subscripts distinguish between cloud and molecular backscatter and extinction Fernald [13]. As the Klett solution applies strictly to a one-component atmosphere we introduce α' and P' in order to account for the mixed contributions from cloud/aerosols and molecular scattering Fernald [13]. If we define

$$\alpha'(z) = \alpha_c(z) + S(z)\beta_{m,\pi}(z), \quad (4.2)$$

and

$$P'(z) = SP(z)e^{2 \int_0^z (\alpha'_m(z')) dz'} e^{-2 \int_0^z (S\beta_m(z')) dz'}. \quad (4.3)$$

Then Equation 4.1 can be recast as

$$P'(z) = \frac{C_{lid}}{S(z)} \alpha'(z) e^{(-2 \int_0^z \alpha'(z') dz')}, \quad (4.4)$$

which has the general form of the single-component lidar equation and has the well-know solution.

In order to calculate the optical cloud extinction coefficient, α' , we invert Equation 4.1 following the analytical solution to the lidar equation proposed by Klett [6].

$$\alpha'(z) = \frac{\frac{P'(z)z^2}{P'(z_0)z_0^2}}{\frac{1}{\alpha'_0} + 2 \int_z^{z_0} \left(\frac{P'(z)z^2}{P'(z_0)z_0^2} \right) dz'}, \quad (4.5)$$

where:

$$\alpha'_0(z_0) = \alpha_c(z_0) + S\beta_{m,\pi}(z_0). \quad (4.6)$$

S is the extinction-to-backscatter ratio ($S = \alpha(z)/\beta_\pi(z)$ here assumed to be range independent within the cloud) and for the water clouds and wavelengths in the range from 200 to 1064 nm it is around 16 sr [14]. α'_0 is the extinction coefficient at a reference height z_0 . Following the method established by Klett [6] and later Fernald [13] we estimate the value of the extinction coefficient at the far end of the range interval to retrieve the full profile of the extinction coefficient. This method was tested for cloudy and foggy conditions and proved appropriate for retrieving the extinction values and it shows small dependence on the estimated extinction boundary value (α'_0) when the optical thickness of the range interval is increasing [9, 15].

Although the principle of this method of lidar signal inversion is straightforward, there is a number of issues that must be addressed to ensure accurate results. Section 4.4.1 outlines these difficulties and presents possible ways of overcoming them. In this work we make use of simulated lidar signals for which the 'true' extinction profiles are know. The simulations include the effects of realistic cloud structure, the effects of finite lidar range resolution and lidar multiple-scattering.

4.3. ECSIM Simulations

To evaluate the retrieval of the cloud extinction we use synthetic signals produced using the lidar Monte-Carlo radiative transfer model component of the Earth-CARE simulator (ECSIM) which has been modified for ground-based simulations [16]. ECSIM is a tool to simulate measurements of four instruments, namely: the 94-GHz cloud profiling radar, the high spectral resolution lidar at 353 nm, the multi-spectral imager and the broad-band radiometer. The lidar model takes into account polarization, multiple-scattering and the effects of finite lidar range resolution. The ECSIM radar model was also used in this paper in an ancillary role. To retrieve

information about the cloud extinction we only need information from lidar. However, information from radar can be used for a further analysis of the scene. Radar can add the capability to identify regions of drizzle. It can also penetrate through a liquid water cloud and hence is useful for establishing the height of the cloud top. To create the scene used in this work, a liquid water content (LWC) field was generated by a Large Eddy Simulation (LES) and introduced to ECSIM. The LES case used was corresponding to one from the FIRE campaign [17]. The ECSIM simulation used specifically an output from the Dutch Atmospheric LES model (DALES) [18]. DALES utilizes a two-moment bulk scheme to model precipitation [19], where condensed water is qualified as either cloud water or precipitation and the number density of cloud droplets is prescribed. The ECSIM scene is created based on a snapshot of parameters extracted from DALES. Those parameters include temperature, pressure, non-precipitable cloud water, precipitation water content and precipitation droplet number density. Further, an explicit droplet size distribution (DSD) is needed to create an ECSIM scene. As DALES does not provide DSDs, imposed DSDs were used, based on the DALES output. The precipitation mode DSD was based on the one from Khairoutdinov and Kogan [19]. The cloud mode DSDs were found by assuming modified gamma type distribution with a width parameter of 5 and assuming a constant cloud-number density, the effective radius of the distributions was then calculated using the model LWC fields.

Figure 4.1 presents the cross section of the Radar Reflectivity Factor and the Attenuated Backscatter Coefficient of the used cloud scene. For this study we performed two simulations based on the same DALES output. One of the cloud scenes was made to simulate Attenuated Backscatter Coefficient with the inclusion of multiple-scattering effects (referred to later in the text as B_{MS}) and the second simulation was made for the single scattering Attenuated Backscatter Coefficient (referred to later in the text as B_{SS}). This allowed us to directly compare the impact of the multiple-scattering on the retrieved values of the extinction coefficient, as well as evaluate the correction for the multiple-scattering presented in Section 4.4.1.

4.4. Inversion results

4.4.1. Difficulties in inversion steps

Defining the normalization interval

In order to obtain a profile of the optical cloud extinction from lidar returns we need to invert the received power (Eq. 4.1) into a cloud optical extinction coefficient as explained in Sec. 4.2. Following the solution proposed by Klett [15] it is necessary to define the range interval where the signal can be normalized. The value of extinction, α'_0 , is estimated at a certain height, z_0 , based, on the slope of the least square straight line fitted to the curve $ATB = ATB(z)$. The value of α'_0 is calculated as follows

$$\alpha'_0 = -\frac{1}{2} \frac{d \ln ATB}{dz}, \quad (4.7)$$

where ATB is the Attenuated Backscatter Coefficient ($ATB(z) = P(z)z^2$) and dz is the range resolution. Figure 4.2 presents the profile of the cloud optical extinction retrieved based on the slope method. It shows clearly that the slope method is not

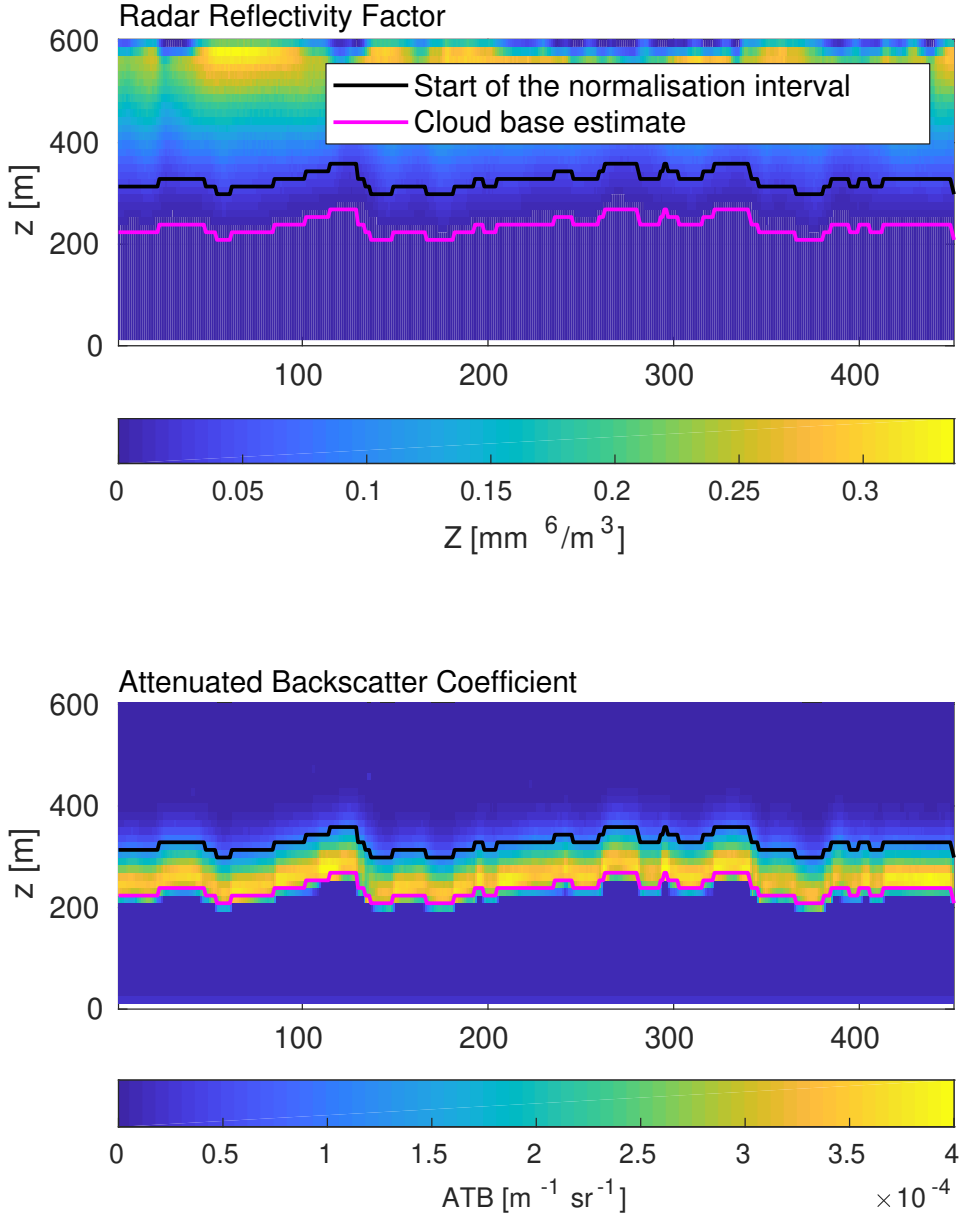


Figure 4.1: Cross section of the Radar Reflectivity Factor (top panel) and Attenuated Backscatter Coefficient (bottom panel) of the cloud scene produced with the ECSIM simulator. The magenta line indicates the estimate of the cloud base height and the black line indicated the beginning of the normalization interval.

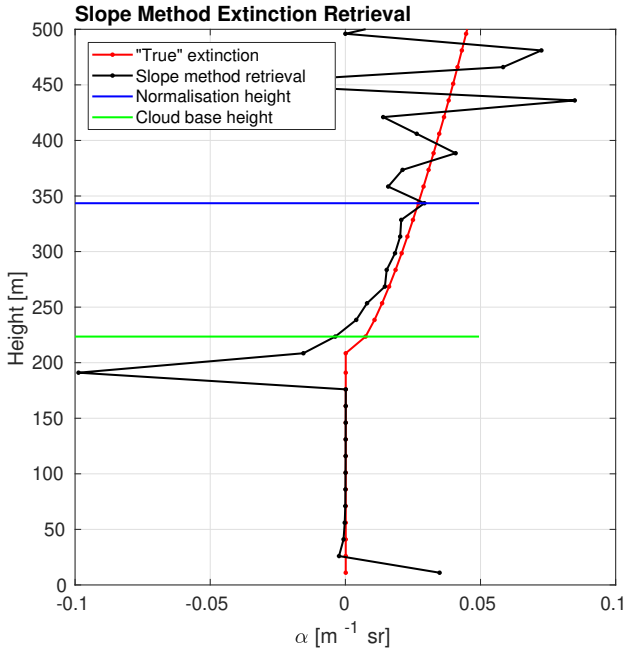


Figure 4.2: Profile of the extinction coefficient retrieved based on the slope method (Eq. 4.7) and the true extinction profile calculated from ECSIM.

accurate at the cloud base and the retrieved values get closer to the true extinction only at a certain height within the cloud. This is in accordance with a proposition by [6], who postulated that the normalization height z_0 where the value of α'_0 is estimated should be located at the far end of the cloud.

Another important aspect in deciding on the height of the normalization interval is the profile of the Attenuated Backscatter Coefficient (*ATB*). In order to calculate α'_0 , *ATB* at the chosen height has to be still usable, meaning that the noise level cannot be too high. Figure 4.3 presents the signal profile with marked normalization interval. Note that the interval is above the peak of the signal and just before signal starts to be noisy or lost. In this study we chose a threshold for the *ATB* usability in the normalization interval at Signal-to-Noise Ratio (*SNR*) of 20. We tested the sensitivity of the inversion method to different values of *SNR* and found that values below 20 tend to influence the retrieval in the higher parts of the cloud. The first four bins within the cloud (up to 60 m within the cloud) are only affected by a mean error increase of 3%. If *SNR* is below 20 then the normalization interval has to be set at a lower height.

Correcting the multiple-scattering

Measurements of water clouds by lidar backscatter always involve some contribution from multiple-scattering. In this study we use the multiple-scattering cor-

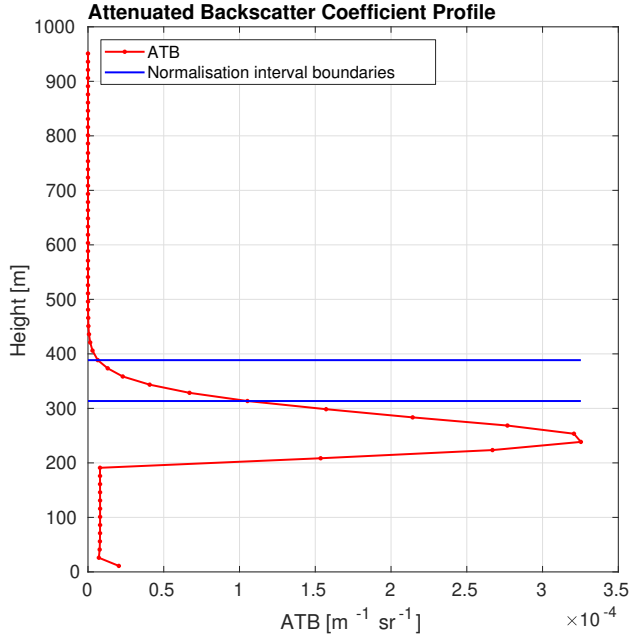


Figure 4.3: Profile of the Attenuated Backscatter Coefficient and boundaries of the normalisation interval.

rection based on the accumulated depolarization ratio (δ_{acc}) introduced by Hu *et al.* [11] and further demonstrated by Cao *et al.* [20]. Lidar multiple-scattering occurring in water clouds can be linked to the depolarization ratio. At 180° backscatter direction single scattering of spherical droplets retains the polarization of the incident light. However, scattering at different scattering angles changes the polarization state. For the liquid water clouds the depolarization of the signal can be attributed to the multiple-scattering [21].

Based on the above described characteristics of water clouds and lidar backscatter Hu *et al.* [11] described a relation between the linear depolarization of the backscatter signal and the fraction of multiple-scattering present in that signal. Based on the Monte Carlo simulations of the multiple-scattering signals for numerous scenarios and different fields-of-view they derived the following relation:

$$A_S(z) = \frac{I_S(z)}{I_T(z)} \approx \frac{(1 - \delta_{acc}(z))^2}{(1 + \delta_{acc}(z))^2}, \quad (4.8)$$

where $I_S(z)$ is the integrated range-corrected single scattering signal and $I_T(z)$ is the integrated, range-corrected total-scattering signal (single and multiple-scattering). Both signals are integrated between the cloud boundaries, where cloud base height is established based on the lidar measurements and we use the top of the normalization interval instead of the cloud top as measurements above that height are no longer relevant. $\delta_{acc}(z)$ is the accumulated depolarization ratio. It can be calculated

Table 4.1: Mean error and accuracy of the cloud optical thickness extinction retrieval for different heights above the cloud base. Data is retrieved by inverting simulated single scattering signal (B_{SS}) signal with α'_o estimate calculated from Eq. 4.7. Results from two inversions are presented: one without any correction and one with the application of the resolution correction calculated from Eq. 4.12 and 4.13 (noted with the subscript *RES*)

Distance from cloud base	$A_{B_{SS}}$	$E_{B_{SS}}$	$A_{B_{SS} \text{ with RES}}$	$E_{B_{SS} \text{ with RES}}$
0.0	92.67%	8.72%	93.21%	8.28%
15.0	92.04%	8.72%	92.76%	8.07%
30.0	93.15%	6.99%	94.23%	5.96%
45.0	93.69%	6.35%	95.11%	4.97%
60.0	94.37%	5.63%	96.26%	3.80%
75.0	94.49%	5.51%	96.76%	3.28%
90.0	94.48%	5.52%	97.08%	2.93%

from the parallel and perpendicular components of the total backscattering signal:

$$\delta_{acc}(z) = \frac{I_{T,\perp}(z)}{I_{T,\parallel}(z)}, \quad (4.9)$$

where $I_{T,\perp}(z)$ is the total integrated perpendicular backscattered signal and $I_{T,\parallel}(z)$ is the total integrated parallel backscattered signal.

In order to calculate the signal corrected for the multiple signal, in other words the signal contributed only to the single scattering ATB_{SS} , we use the following formula:

$$ATB_{SS}(z) = A_S(z)ATB_{MS}(z) + I_T(z) \frac{dA_S}{dz}, \quad (4.10)$$

where A_S is the correction factor calculated from Eq. 4.8, ATB_{MS} is the total range corrected signal, the $I_T(z)$ is the integrated, range-corrected total-scattering signal and $\frac{dA_S}{dz}$ is the derivative of the correction factor from Eq. 4.8. The last term of Eq. 4.10 can be used to evaluate the depolarization both in simulated and real conditions. The value of $\frac{dA_S}{dz}$ should always be negative within the cloud because higher within the cloud more multiple-scattering occurs and a smaller part of the signal can be associated only with the single scattering.

Figure 4.4 presents samples of retrieved profiles with and without the correction for the multiple-scattering (noted as *MS* correction) plotted against the cloud optical thickness (τ). Applying the MS correction improves greatly the accuracy and minimizes the error of the retrieved profiles (for more detailed information see Table 4.2). Based on the data analysis performed for this paper we can conclude that multiple-scattering correction has a big impact on the accuracy of the retrieved cloud optical extinction.

Effects of the range resolution

The finite range resolution of the lidar signal is another factor that influences the final results of the inversion. The range resolution of lidar varies depending on

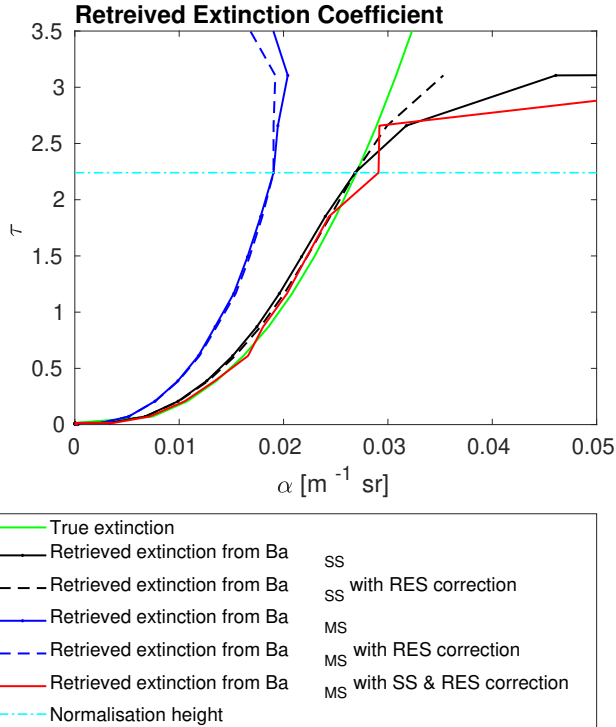


Figure 4.4: Profiles of the retrieved cloud optical extinction retrieved through an inversion of the signal with different corrections. The green line represents the true extinction calculated with the ECSIM. The black solid line represents the extinction profile retrieved without any corrections from the modeled single scattering attenuated backscatter. The dashed black line represents the extinction profile retrieved from the modeled single scattering attenuated backscatter with the resolution correction. The blue solid line represents the extinction profile retrieved without any corrections from the modeled multiple-scattering attenuated backscatter. The dashed blue line represents the extinction profile retrieved from the modeled multiple-scattering attenuated backscatter with the resolution correction. The red line represents the extinction profile retrieved from the modeled multiple-scattering attenuated backscatter with the resolution and multiple-scattering correction. The dashed cyan line indicates the beginning of the normalization interval.

the system and the larger it is the higher might be its impact on the final inversion results. Problems with the resolution of lidar were mentioned before [22], but were never really studied and no solution to the problem was proposed so far.

The difficulty associated with the range resolution occurs since practical lidar data is always acquired at a finite resolution and thus must be interpreted using a discrete form of solution to the lidar equation. The continuous form of the equation 4.5 is often naively transformed into a discrete form, where the integration is transformed into a summation using e.g. the trapezoid rule, yielding

$$\alpha'_i = \frac{\frac{P'_i z_i^2}{P'_{i_0} z_{i_0}^2}}{\frac{1}{\alpha'_0} + P'_i z_i^2 \Delta z + 2 \sum_{i+1}^{i_0-1} P'_i z_i^2 \Delta z + P'_{i_0} z_{i_0}^2 \Delta z}. \quad (4.11)$$

Although this is a common practice when transforming continuous equation to discrete form in algorithms, it may not be sufficiently accurate. If the value of $\alpha' \Delta z$ is small enough, then the approximation by the use of the trapezoid rule is accurate and the resulting value of α' corresponds to the bin mid-point. However if that value is large, the applied approximation is not correct anymore. The detailed explanation of the calculations is presented in 4.6.

Based on the calculations for the mid-point of the bin we define the resolution correction (RES and RES_2) as follows:

$$RES(z) = \frac{e^{\alpha'(z)\Delta z}}{e^{\alpha'(z)\Delta z} - e^{-\alpha'(z)\Delta z}}, \quad (4.12)$$

and

$$RES_2(z) = \frac{2\alpha'(z)\Delta z}{e^{\alpha'(z)\Delta z} - e^{-\alpha'(z)\Delta z}}, \quad (4.13)$$

where $\alpha'(z)$ is the retrieved cloud optical extinction and Δz is the height resolution. In order to apply this correction factor we need to perform the inversion in two steps. Firstly, we invert the lidar signal and apply the multiple-scattering correction. The resulting optical cloud extinction (α) from the first inversion is used in the range resolution correction (Eq. 4.12 and 4.13) and then the corrected signal is inverted again.

Figure 4.4 presents the retrieved profiles of α with the multiple-scattering correction (denoted as MS) and with the multiple-scattering correction together with the range resolution correction (denoted as $MS \& RES$). We observe that while the MS correction on its own improves the retrieval greatly, after application of the RES correction values of α are closer to the true value of extinction coefficient. The importance of the resolution correction can be easily presented when we inverted the simulated single scattering signal (B_{SS} , as mentioned in Section 4.3). Table 4.2 presents error and accuracy of the inversion results (as described in Section 4.4.3).

4.4.2. Estimating cloud base height

Although it is not directly connected to the inversion procedure, an accurate estimation of the cloud base height is also a challenging problem in cloud obser-

Table 4.2: Mean error and accuracy of the cloud optical thickness extinction retrieval for different heights above the cloud base. Data is retrieved by inverting simulated multiple-scattering signal (B_{MS}) signal with α' estimate calculated from Eq. 4.7. Results from four inversions are presented: one without any correction, one with the application of the resolution correction calculated from Eq. 4.12 and 4.13 (noted with the subscript RES), one with the multiple-scattering correction calculated from Eq. 4.8 (noted with the subscript MS) and the last one with both the resolution and the multiple-scattering correction (noted with the subscript RES&MS)

Distance from cloud base	$A_{B_{MS}}$	$E_{B_{MS}}$	$A_{B_{MS} \text{ with RES}}$	$E_{B_{MS} \text{ with RES}}$	$A_{B_{MS} \text{ with MS}}$	$E_{B_{MS} \text{ with MS}}$	$A_{B_{MS} \text{ with RES\&MS}}$	$E_{B_{MS} \text{ with RES\&MS}}$
0.0	59.25%	40.77%	72.14%	27.91%	99.50%	5.58%	98.71%	5.77%
15.0	69.40%	30.61%	71.49%	28.53%	98.22%	4.55%	97.79%	4.77%
30.0	71.79%	28.21%	72.86%	27.14%	98.35%	3.14%	98.55%	3.06%
45.0	72.87%	27.13%	73.48%	26.52%	99.00%	2.73%	99.74%	2.52%
60.0	72.65%	27.35%	73.42%	26.58%	96.11%	4.34%	97.30%	3.50%
75.0	73.12%	26.88%	73.96%	26.04%	95.83%	4.67%	97.48%	3.72%
90.0	72.50%	27.50%	73.72%	26.28%	94.44%	5.93%	96.37%	4.66%

vation. In this study we use the peak of the lidar perpendicular signal to evaluate the cloud base height. Lidar power ($P(z)$, Eq.4.1) from a depolarization lidar can be divided into the parallel ($P(z)_{\parallel}$) and perpendicular power ($P(z)_{\perp}$). In every profile we find the peak of the perpendicular power ($P(z)_{\perp max}$) and estimate the cloud base to be at the height where $P(z)$ is equal or greater than $P(z)_{\perp max}$ divided by ten. We found that this estimate predicts the height of cloud base with a good accuracy for the liquid water clouds. Figure 4.1 presents the Radar Reflectivity Factor and the Attenuated Backscatter Coefficient for the scene used in this study. Both panels present the estimate of the cloud base height marked with a magenta line. Examining the panel with the *ATB* we see that our estimate is a good approximation.

4.4.3. Signal inversion error and accuracy

In this study we use the ECSIM cloud scene to test the accuracy and estimate the error of the lidar signal inversion. The dataset from ESCIM gives us information about the true value of optical extinction coefficient within the cloud. Thanks to that we can calculate the percent error and the accuracy of the inversion method by comparing the retrieved value to the true (simulated) value of the optical extinction coefficient. For those calculations we use the following formulas:

$$E_{B_{SS}orB_{MS}} = \frac{\alpha_{retrieved} - \alpha_{simulated}}{\alpha_{simulated}} * 100\%, \quad (4.14)$$

to estimate the percent error, and:

$$A_{B_{SS}orB_{MS}} = \frac{\alpha_{retrieved}}{\alpha_{simulated}} * 100\%, \quad (4.15)$$

to estimate the accuracy, where the subscript B_{SS} is used when we are inverting signal from the single scattering simulation and the subscript B_{MS} is used for the simulations from the multiple-scattering simulations. For the whole dataset the mean values for each height above the cloud base are presented in Table 4.1 for B_{SS} and in Table 4.2 for B_{MS} .

As we indicated before, values retrieved at the cloud base (defined as being 0 m from the cloud base in Table 4.1 and 4.2) are the ones with the biggest percent error. This stems from the difficulty in the signal inversion at very small values of cloud optical extinction. We observe a great improvement of the accuracy of the inversion further within the cloud. We present values of the inversion error and accuracy for the retrieval without any correction and for the retrieval only with the resolution correction ($A_{B_{MS} with RES}$ and $E_{B_{MS} with RES}$), only with the multiple-scattering correction ($A_{B_{MS} with MS}$ and $E_{B_{MS} with MS}$) and with both the multiple-scattering and the resolution correction ($A_{B_{MS} with RES\&MS}$ and $E_{B_{MS} with RES\&MS}$).

For the results of the inversion of the B_{SS} signal we tested how can the resolution correction improve the results of the retrieval. Table 4.1 presents the mean error and accuracy calculated at different levels within the cloud. We observed an increased impact of the resolution correction deeper within the cloud. At a distance 45 to 90 m from the cloud base the resolution correction almost doubles the accuracy. This is mostly due to an increase in the value of cloud optical extinction

(α). As we explain in the Appendix 4.6, the resolution correction is less relevant for small values of α . Inversion of the signal with the simulated multiple-scattering (B_{MS}), and thus far more resembling actual measurements, is understandably less accurate. Table 4.1 presents mean error and accuracy of the retrieved cloud optical extinction for different heights above the cloud base. Inversion without any correction had a mean error ranging from 40% at cloud base to 26% in the cloud. We observed that with the resolution correction only the error can be improved by up to 3%. The correction for the multiple-scattering has a much bigger impact, it improve the inversion error by around 35% at the cloud base and by 20% higher within the cloud. By combining the resolution and multiple-scattering correction the error of the inversion can be improved to between 6% at the cloud base and 3-4% within the cloud. We observed that the inversion is most accurate between 30 and 60 m within the cloud. Figure 4.5 presents the cross-section of the retrieval percent error of the cloud optical extinction for the inversion of simulated multiple-scattering signal with the inclusion of the resolution and multiple-scattering correction. The increase of the error above 60 m from the cloud base mainly is due to an underestimation of the value of cloud optical extinction at the normalisation height (α_0). The accuracy of the retrieval is connected to the cloud optical thickness. Figure 4.6 presents scatter plots of the retrieved values of α with the multiple-scattering and range resolution correction plotted against the modelled ones. The data is divided by the value of the optical thickness, τ , where

$$\tau(z) = \int_0^h \alpha'(z) dz, \quad (4.16)$$

α is the cloud optical thickness and h is cloud depth. Every panel includes an imposed red line which represents an equality between the modeled and retrieved values. We also used a colour scaling, where the color bar represents the value of cloud optical extinction at every point. The error (Eq. 4.14) and accuracy (Eq. 4.15) for each bin on the optical thickness is also presented. We observed that the inversion method works best for the values of τ between 0.6 and 1.05. The error for values of τ above 1.5 is higher and the retrieved cloud optical extinction is underestimated. The probable cause of this behaviour of the retrieval is the loss of a signal with the increase of the cloud optical thickness. For the optical thickness below 0.6 and further below 0.15 the important factor influencing the accuracy of the retrieval is the estimation of the cloud base region.

Figure 4.5 presents the cross section of the cloud optical thickness and the retrieval percent error. Here again we can clearly see that the percent error is highest close to the cloud base, ranging between 8%-15%, and deeper within the cloud it rarely exceeds 7%. This means that when inverting the lidar signal it is important to carefully examine the first range above the cloud base.

4.4.4. Impact of α_0 estimation

Klett [6] stated that the value of α'_0 does not influence much the final results of the inversion. In our study we tested this statement by performing inversion with the actual value of extinction at the normalisation height z_0 instead of the

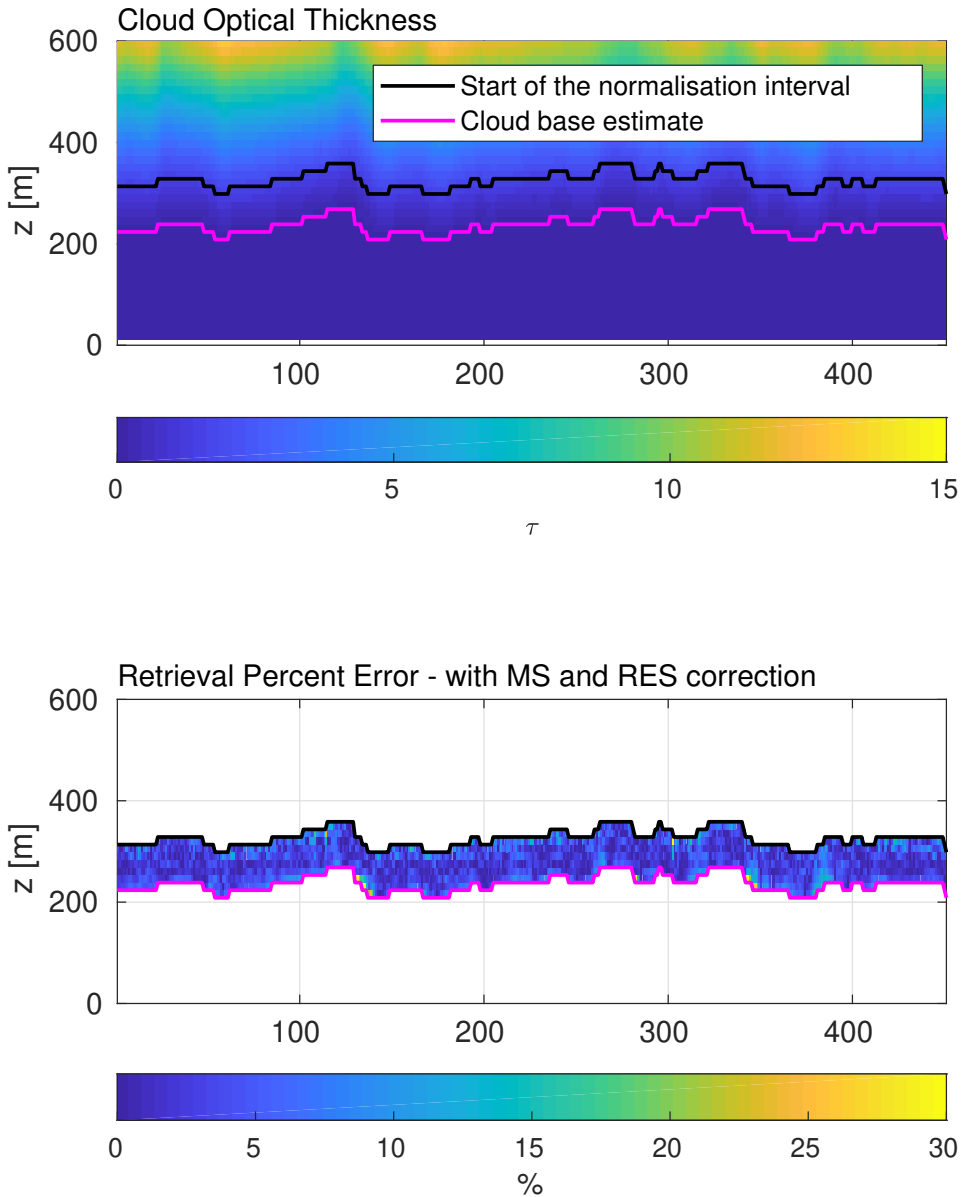


Figure 4.5: Cross section of the Cloud Optical Thickness (top panel) and Retrieval Percent Error of the cloud optical extinction retrieved with the multiple-scattering and range resolution correction (bottom panel). The magenta line on both panels represents the estimated height of the cloud base and the black line is the beginning of the normalization interval.

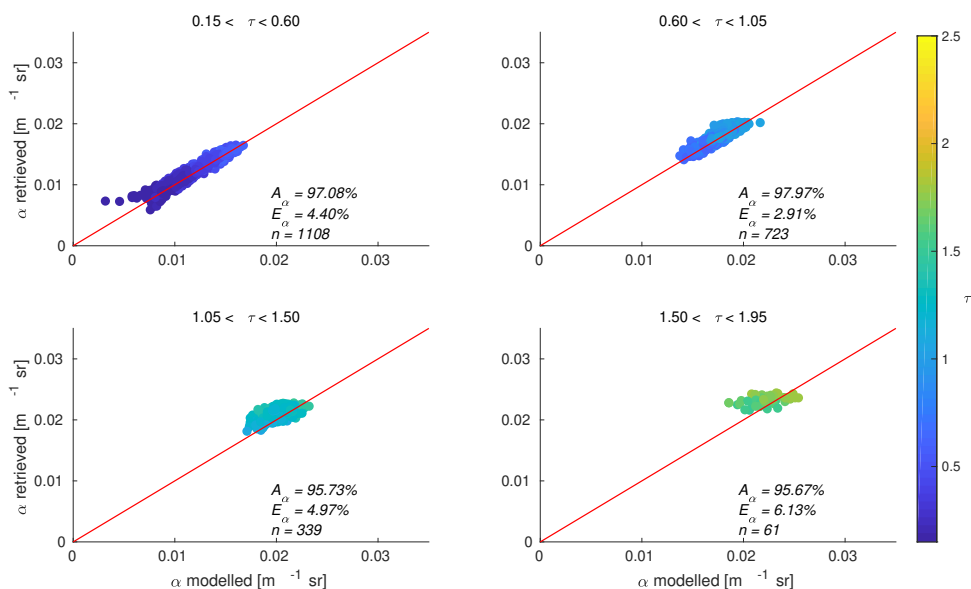


Figure 4.6: Scatter plots of the retrieved cloud optical extinction (with the multiple-scattering and range resolution correction) versus the modeled cloud optical extinction from the ECSIM divided into panels depending on the value of the optical thickness. The red line is imposed and represents the equality between the modeled and retrieved values. The colorbar represents the value of the cloud optical thickness at each point. The error (Eq. 4.14) and accuracy (Eq. 4.15) for each bin of the optical thickness is also presented.

Table 4.3: Mean error and accuracy of the cloud optical thickness extinction retrieval for different heights above the cloud base. Data is retrieved by inverting simulated multiple-scattering signal (B_{MS}) with both the resolution and the multiple-scattering correction, with α_0 equal to the true extinction at the normalization height z_0 (noted as α_{true}) and in the second case with α_0 estimate calculated from Eq. 4.7 (noted as α_{slope}).

Distance from cloud base	$A_{B_{MS}}$ for α_{true}	$E_{B_{MS}}$ for α_{true}	$A_{B_{MS}}$ for α_{slope}	$E_{B_{MS}}$ for α_{slope}
0.0	98.71%	5.77%	98.94%	5.72%
15.0	97.79%	4.77%	98.03%	4.69%
30.0	98.55%	3.06%	98.94%	2.98%
45.0	99.74%	2.52%	100.27%	2.47%
60.0	97.30%	3.50%	98.20%	2.97%
75.0	97.48%	3.72%	98.84%	2.92%
90.0	96.37%	4.66%	98.12%	3.24%

value calculated from the slope method (4.7). The results of this inversion are presented in Table 4.3. The error for the inversion with the multiple-scattering and resolution correction is improved by around 0.5%. The error improvement is more significant for the values retrieved above 60 m from the cloud base. This is due to the underestimation of the value of α'_0 with the slope method (Figure 4.2). We also tested the accuracy of the calculated α'_0 by comparing it to the actual value of α at the normalization height z_0 . The mean accuracy of α'_0 for the whole data set was 95%, with the minimum accuracy of 89% and the maximum one of 112%.

4.5. Conclusions

In this paper we presented a method of lidar signal inversion for the retrieval of the cloud optical extinction in the cloud base region. This method was first presented by Klett [6]. We showed that with the correction for the multiple-scattering within the cloud and the resolution correction this method can be successfully used for the retrieval of the cloud optical extinction. Both those corrections are essential to improve the accuracy of the retrieved extinction profile and minimize the error. We presented the performance of the retrieval based on the synthetically created cloud scene where responses of the lidar to a specific cloud conditions were simulated. Even though in some case the cloud base was not varying much in height, the analyzed data indicated that signal inversion close to the cloud base (specifically at the range of the detected cloud base) is prone to error. The retrieval of the cloud optical extinction works better at higher values of the optical thickness. It is therefore our recommendation to use only data points located at least one gate range above the detected cloud base height. We also showed that the approximation of α'_0 calculated with the slope method can be used as an estimation of actual cloud optical extinction at the normalization height. More importantly, improving the value of α'_0 by using the actual extinction at the normalization height does not improve the retrieved values significantly if the correction for the multiple-scattering and range resolution is implemented.

We showed that the inversion of the lidar signal with the proposed corrections yields a good estimate of the cloud extinction. Not only is this method fast, but also, because of the use of a standard backscatter depolarization lidar, can be applied to multiple systems and used operationally. Through a link between cloud microphysical properties and the optical extinction this can provide a valuable dataset to be used in the studies of cloud microphysics and impacts of clouds on the climate.

4.6. Appendix A - Derivation of the resolution correction

The difficulty associated with the range resolution occurs since practical lidar data is always acquired at a finite resolution and thus must be interpreted using a discrete form of the lidar equation. The single-scattering lidar continuous equation, in term of the range corrected signal $B(z)$ can be defined as:

$$B(z) = C \alpha'(z) e^{-2 \int_0^z \alpha(z') dz'}, \quad (4.17)$$

where C is the lidar constant, α' is the cloud optical extinction and z is range or in terms of optical thickness τ as:

$$B(z) = C \frac{d\tau}{dz} e^{-2\tau(z)}, \quad (4.18)$$

where τ is the cloud optical thickness. In the discrete form, backscatter signal for one point B_i is defined as

$$B_i = \int_{z_i - \frac{\Delta z}{2}}^{z_i + \frac{\Delta z}{2}} B(z) dz. \quad (4.19)$$

Applying the form from the Eq. 4.18 we can say that:

$$B_i = -\frac{c}{2} e^{-2\tau(z)} \Big|_{z_i - \frac{\Delta z}{2}}^{z_i + \frac{\Delta z}{2}}, \quad (4.20)$$

which is equal to

$$B_i = \frac{c}{2} \left[e^{-2\tau(z_i)} - e^{-2\tau(z_i + \frac{\Delta z}{2})} + e^{-2\tau(z_i - \frac{\Delta z}{2})} - e^{-2\tau(z_i)} \right] \quad (4.21)$$

and

$$B_i = \frac{c}{2} [B_{i,1} + B_{i,2}], \quad (4.22)$$

as illustrated on figure 4.7. The difference between B_i and $B_{i,1}$ can be then calculated

$$\frac{B_i}{B_{i,1}} = - \left(\frac{1 - e^{-2(\tau(z + \frac{\Delta z}{2}) - \tau(z))}}{1 - e^{-2(\tau(z - \frac{\Delta z}{2}) - \tau(z))}} \right) + 1. \quad (4.23)$$

If we assume that

$$\tau(z + \frac{\Delta z}{2}) + \tau(z) \approx \frac{\alpha' \Delta z}{2} \quad (4.24)$$

and

$$\tau(z + \frac{\Delta z}{2}) - \tau(z) \approx -\frac{\alpha' \Delta z}{2} \quad (4.25)$$

Eq 4.23 becomes

$$\frac{B_i}{B_{i,1}} = -1 \left(\frac{1 - e^{-\alpha' \Delta z}}{1 - e^{\alpha' \Delta z}} \right) = -\frac{e^{\alpha \Delta z} - e^{-\alpha' \Delta z}}{1 - e^{\alpha' \Delta z}}. \quad (4.26)$$

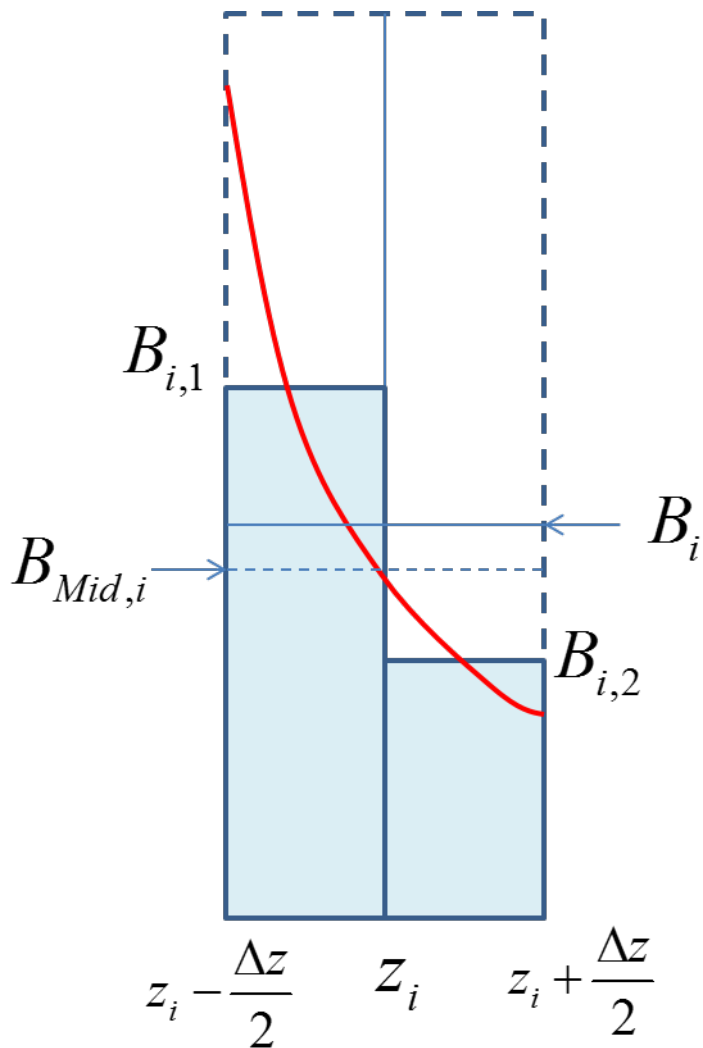


Figure 4.7: Illustration of the discrete form of the lidar equation.

We can then calculate $B_{i,1}$,

$$B_{i,1} = B_i \left(\frac{e^{\alpha' \Delta z}}{e^{\alpha' \Delta z} - e^{-\alpha' \Delta z}} \right) \quad (4.27)$$

and thus we define the resolution correction RES which equals

$$RES = \frac{e^{\alpha' \Delta z}}{e^{\alpha' \Delta z} - e^{-\alpha' \Delta z}}. \quad (4.28)$$

In cases when $\alpha' \Delta z$ will be large:

$$B_{i,1} \approx B_i \left(\frac{e^{\alpha' \Delta z}}{\alpha' \Delta z} \right) \approx B_i, \quad (4.29)$$

and if $\alpha' \Delta z$ will be small:

$$B_{i,1} \approx B_i \left(\frac{\alpha' \Delta z}{2\alpha' \Delta z} \right) \approx \frac{1}{2} B_i. \quad (4.30)$$

The value of RES will be around 0.5 and it's applied to the lidar power signal, specifically in the calculation of the integral in the term $\int_z^{z_0} \left(\frac{P'(z)z^2}{P'(z_0)z_0^2} \right) dz'$ in Eq. 4.5, where the usual value of $\frac{1}{2}$ used in the trapezoidal rule of integration is replaced by a corresponding RES . If that values of RES will be higher or smaller we have to compensate so that the equalities of Eq. 4.6, specifically $[B_{i,1} + B_{i,2}]_r$, are not greater than one. For that we derived the second part of the resolution correction RES_2 . RES_2 is defined as

$$RES_2 = \frac{2\alpha' \Delta z}{e^{\alpha' \Delta z} - e^{-\alpha' \Delta z}}. \quad (4.31)$$

The value of RES_2 cannot be higher than 1. RES_2 is applied in the first term of Eq. 4.5, so that $\frac{P'(z)z^2}{P'(z_0)z_0^2}$ becomes $\frac{(P'(z)z^2)RES_2(z)}{(P'(z_0)z_0^2)RES_2(z_0)}$.

References

- [1] K. Sarna, D. P. Donovan, and H. W. J. Russchenberg, *Estimating optical extinction of liquid water clouds in the cloud base region*, *Atmospheric Measurement Techniques Discussions* **2021**, 1 (2021).
- [2] R. T. H. Collis, *Lidar: A new atmospheric probe*, *Quarterly Journal of the Royal Meteorological Society* **92**, 220 (1966).
- [3] G. Fiocco and L. D. Smullin, *Detection of Scattering Layers in the Upper Atmosphere (60–140 km) by Optical Radar*, *Nature* **199**, 1275 (1963).
- [4] D. Müller, U. Wandinger, D. Althausen, I. Mattis, and A. Ansmann, *Retrieval of Physical Particle Properties from Lidar Observations of Extinction and Backscatter at Multiple Wavelengths*, *Applied Optics* **37**, 2260 (1998).
- [5] D. D. Turner, *Arctic Mixed-Phase Cloud Properties from AERI Lidar Observations: Algorithm and Results from SHEBA*, *Journal of Applied Meteorology* **44**, 427 (2005).
- [6] J. D. Klett, *Stable analytical inversion solution for processing lidar returns*. *Applied optics* **20**, 211 (1981).
- [7] a. Kokhanovsky, *Optical properties of terrestrial clouds*, *Earth-Science Reviews* **64**, 189 (2004).
- [8] A. McComiskey and G. Feingold, *The scale problem in quantifying aerosol indirect effects*, *Atmospheric Chemistry and Physics* **12**, 1031 (2012).
- [9] W. Carnuth and R. Reiter, *Cloud extinction profile measurements by lidar using {Klett}'s inversion method*, *Appl. Opt.* **25**, 2899 (1986).
- [10] F. Rocadenbosch, A. Comerón, and D. Pineda, *Assessment of Lidar Inversion Errors for Homogeneous Atmospheres*, *Applied Optics* **37**, 2199 (1998).
- [11] Y. Hu, Z. Liu, D. Winker, M. Vaughan, V. Noel, L. Bissonnette, G. Roy, and M. McGill, *Simple relation between lidar multiple scattering and depolarization for water clouds*. *Optics letters* **31**, 1809 (2006).
- [12] G. Roy and X. Cao, *Inversion of water cloud lidar signals based on accumulated depolarization ratio*. *Applied optics* **49**, 1630 (2010).
- [13] F. G. Fernald, *Analysis of atmospheric lidar observations;*, *Applied Optics* **23** (1984).
- [14] J. E. Yorks, D. L. Hlavka, W. D. Hart, and M. J. McGill, *Statistics of {Cloud} {Optical} {Properties} from {Airborne} {Lidar} {Measurements}*, *J. Atmos. Oceanic Technol.* **28**, 869 (2011).
- [15] J. D. Klett, *Lidar inversion with variable backscatter/extinction ratios*, *Appl. Opt.* **24**, 1638 (1985).

- [16] D. P. Donovan, H. Klein Baltink, J. S. Henzing, S. R. de Roode, and a. P. Siebesma, *A depolarisation lidar-based method for the determination of liquid-cloud microphysical properties*, *Atmospheric Measurement Techniques* **8**, 237 (2015).
- [17] B. A. Albrecht, D. A. Randall, and S. Nicholls, *Observations of marine stratocumulus clouds during FIRE*, *Bulletin - American Meteorological Society* **69**, 618 (1988).
- [18] T. Heus, C. C. van Heerwaarden, H. J. J. Jonker, A. Pier Siebesma, S. Axelsen, K. van den Dries, O. Geoffroy, A. F. Moene, D. Pino, S. R. de Roode, and J. Vilà-Guerau de Arellano, *Formulation of the Dutch Atmospheric Large-Eddy Simulation (DALES) and overview of its applications*, *Geoscientific Model Development* **3**, 415 (2010).
- [19] M. Khairoutdinov and Y. Kogan, *A New Cloud Physics Parameterization in a Large-Eddy Simulation Model of Marine Stratocumulus*, *Monthly Weather Review* **128**, 229 (2000).
- [20] X. Cao, G. Roy, N. Roy, and R. Bernier, *Comparison of the relationships between lidar integrated backscattered light and accumulated depolarization ratios for linear and circular polarization for water droplets, fog oil, and dust*, *Appl. Opt.* **48**, 4130 (2009).
- [21] K. Sassen and R. L. Petrilla, *Lidar depolarization from multiple scattering in marine stratus clouds*, *Applied Optics* **25**, 1450 (1986).
- [22] B. Evans, *On the Inversion of the Lidar Equation*, Tech. Rep. (Research and Development Branch Department of the National Defence Canada, 1984).

5

Summary and Outlook

5.1. Summary

In this thesis a method of observing and quantifying aerosol-cloud interactions with ground-based remote sensing instruments working in synergy was presented. Aerosol-cloud interactions remain one of the most uncertain contributors in the climate models. The main motivation of this thesis was to propose a scheme that can help reduce that uncertainty by providing continuous measurement and quantification of the aerosol-cloud interactions. The method is based on high-resolution ground based remote sensing instruments. In order to capture the process we use information from Lidar to capture the aerosols background, from radar to capture the cloud properties and from radiometer to ensure that the amount of available water remains the same. The presented scheme was developed specifically for the Cloudnet network. Cloudnet observatories are widely spread through Europe and are able to provide a large coverage of measurement on a converted uniform grid. The presented ACI method utilises Cloudnet categorisation product to select data for a specific target only, namely liquid water clouds and aerosol. In order to decouple the ACI process from a bigger scale meteorological phenomena data is further chosen based on the variation in temperature, pressure and humidity. In Chapter 2 data is analysed on a daily basis and in Chapter 3 an aggregated data set is used. In both cases data is always selected based on the amount of water, for which we use the Liquid Water Path (LWP).

In Chapter 2 data was divided into LWP bins of 10 gm_2 and analysed for a number of days. Data was obtained at the Atmospheric Research Measurements (ARM) Mobile Facility on Graciosa Island, the Azores, Portugal. This specific site was chosen due to an availability of pristine liquid water clouds which are best suited for testing the ACI method. In this study the metric to quantify the aerosol-cloud interactions (ACI_r) was based on the aerosols backscatter measured by lidar and cloud droplet effective radius derived from radar and radiometer observations. It was shown that the impact of aerosols on clouds was strongest for the low level liquid water clouds, with the LWP ranging between 40 and 70 gm_2 . For clouds with a higher amount of water other processes, most probably collision and coalescence become dominant cloud processes.

In Chapter 3 the ACI method was applied to an aggregated data set collected at the CESAR Observatory in the Netherlands. Again the method was only applied to non-precipitating, low level (with a cloud base between 500 and 2000 m above the ground level) liquid water clouds. As in this study was aggregated automatically an additional filter was introduced to ensure that no single points from a specific cloud are taken into the statistics. Only the case where all cloud selection criterias were persisting for at least 30 minutes were considered in the study. The metrics used to quantify aerosol-cloud interactions in this study was ACI_r and additionally ACI_N , which is a metric derived from the aerosols backscatter from lidar and from the cloud droplet number concentration derived from radar and radiometer observations. The calculated values of the ACI_r were in line with the values obtained by similar studies. However the ACI_N metric showed a relevant discrepancy with

previous studies, showing a much lower value than those reported in literature. The reason for that is threefold: the uncertainty of the retrieval of the cloud droplet number concentration ranges between 40 and 60% in itself, further the calculation of the cloud droplet number concentration is performed for the whole cloud and not only for the cloud base region where the ACI process is taking place and lastly comparing with the literature in this case is tricky, as most commonly the data for ACI is collected in the marine environments, which is not the case for Cabauw. In this study the highest values of ACI_r were recorded for the LWP between 60 and 105 gm_{-2} . It was also demonstrated that there is a significant increase in ACI_r when only the cloud updraft regions were considered.

In Chapter 4 a method was presented to estimate cloud optical extinction in the cloud base region. This method is based on lidar measurements and utilises a well established Klett inversion scheme to obtain cloud extinction profile between the cloud base and up to 90 m within the cloud. The retrieval is dependent on the cloud optical thickness: it is most accurate for the cloud optical thickness between 0.15 and 1. The estimation at the cloud base is more difficult. For the height above 90 m the lidar signal is lost and the inversion is no longer possible. This method presents an alternative cloud optical characterisation proxy and can be used in the ACI method described in Chapter 2 and 3. Since the retrieval is based only on the measurements from lidar, it would allow for an even further Overall this thesis showed that it is possible to approximate aerosol-cloud interaction with the ground-based remote sensing instruments. By no means is this an exhaustive method that gives the most accurate results. But it was also not the goal of it. The main goal was to use widely available instruments to make it possible to characterize aerosol-cloud interactions with the same method over a large area. By applying this method to the CLOUDNET network it will be possible to have an estimation of the contribution of the aerosol-cloud interactions over Europe.

5.2. Outlook

The logical follow up of the work presented in this thesis is threefold:

- Extension of the method by the inclusion of the Cloud extinction as a cloud properties proxy. The inversion scheme described in Chapter 4 can be used instead or in addition to the radar measurements in the ACI method. In case both proxies are used a possible cross-validation of the cloud properties would be possible. In case of using only the lidar measurements it would be possible to characterise aerosol-cloud interactions on even more sites, since UV lidars and radiometers are more widely available (and cheaper) instruments than cloud radars.
- Application of the method to the CLOUDNET network and comparison of the results among different sites. As mentioned before, the ACI method was designed for the CLOUDNET data format hence application of this method to multiple sites within the network will be possible. Further, since CLOUDNET

data format is also available for many ARM sites, the method could be further applied. As envisaged this would allow to characterise the aerosol-cloud interactions over a large geographical area.

- Extension of the method to a satellite remote sensing application. One of the upcoming ESA (European Space Agency) missions will enable to apply the described method to the satellite measurements. EarthCARE will carry an atmospheric lidar, cloud profiling radar and radiometer and hence will be capable of characterising aerosol-cloud interactions.

Additionally, during summer 2016 the ASCENSION Island Initiative (ASCI) project in cooperation with KNMI took place. During a month of measurements a UV-lidar was deployed to Ascension Island as an extension of the CLARIFY-2016 campaign (CLOUDS and Aerosol Radiative Impacts and Forcing: Year 2016, lead by the University of Reading). The method described in this study was the driver for starting that campaign and was further modified for that specific application [1].

5

References

- [1] E. V. Tenner, *The UV-LIDAR: A tool for investigating Aerosol-Cloud Interactions A case study on As-cension Island*, Tech. Rep. (2017).

Curriculum Vitæ

Karolina SARNA

05-06-1985 Born in Warsaw, Poland.

Education

- 2004–2008 Bachelor of Science, Environmental Science
Warsaw University of Technology,
Warsaw, Poland
- 2008–2011 Masters of Science, Environmental Science (specialization in Meteorology)
Warsaw University of Technology,
Warsaw, Poland
- 2008–2009 Masters of Science, Environmental Science
Universidad de Salamanca,
Salamanca, Spain
Student exchange programme SOCRATES ERASMUS
- 2012–2016 PhD Atmospheric Physics
Delft University of Technology,
Thesis: Monitoring Aerosol - Cloud Interactions in Liquid
Water Clouds
Promotor: Prof. dr. ir. H. W. J. Russchenberg

Awards

2016 Pieter Langerhuizen Stipendium

List of Publications

7. **Sarna, K.**, Donovan, D. P., and Russchenberg, H. W. J., *Estimating optical extinction of liquid water clouds in the cloud base region*, *Atmos. Meas. Tech. Discuss.* [preprint], in review, (2021).
6. **Sarna, K.**, Russchenberg, H.W.J., *Monitoring aerosol-cloud interactions at the CESAR Observatory in the Netherlands*, *Atmospheric Measurement Techniques*. 10, 5, p. 1987-1997 11 p., (2017).
5. **Sarna, K.**, Russchenberg, H.W.J., *Ground-based remote sensing scheme for monitoring aerosol-cloud interactions*, *Atmospheric Measurement Techniques*. 9, 3, p. 1039-1050 12 p., (2016).
4. **Sarna, K.**, *ACI monitoring: Second release*, *Zenodo* 593226, (2016).
3. **Sarna, K.**, Russchenberg, H.W.J., *A framework for aerosol-cloud interactions monitoring*, *7 th Symposium on Aerosol-Cloud-Climate Interactions*, Phoenix, USA, 4/01/15 - 8/01/15, (2015).
2. **Sarna, K.**, Russchenberg, H.W.J. & Donovan, D.P., 2014, *How can we use lidar and radar to monitor aerosol-cloud interaction?*, *14th conference on atmospheric radiation*, Boston, USA, 7/07/14 - 11/07/14 pp. 1-1 (2014).
1. **Sarna, K.**, Russchenberg, H.W.J., *A framework for cloud - Aerosol interaction study*, *Proceedings of the 9th international symposium on tropospheric profiling*. Cimini, D., Di Girolamo, P., Marzano, FS. & Rizi, V. (eds.). s.l.: ESA, p. 1-4 4 p. (2012).

Acknowledgments

Writing a thesis is a difficult undertaking and although done solitary, there is a great amount of people who contribute to it.

I would like to start by thanking the European Research Council for making this research possible and for all the work they do to support research in general.

I would also like to thank my supervisor Prof. Dr. ir. Herman Russchenberg, who gave me the support I needed to finish this thesis. He gave me the possibility to continue writing my thesis after I left the university and combined the remaining research with a full time work. Due to his steady encouragement and valuable feedback I was able to reach the finish line. Thank you Herman for giving me the space to slowly but steadily finish this work.

I am very grateful to Dr. Dave Donovan for encouraging me to explore new paths in my research. He spend countless hours helping my understand the specifics of lidar and the possibilities to apply its results in my research. He arranged for me to join the team at KNMI on a weekly basis, where not only did I get to work more closely with him, but also had an opportunity to meet other colleagues from KNMI and exchange ideas, which always helped me in moving my research forward. Thank you Dave for being my mentor.

There are any other people within the Geoscience and Remote Sensing department at TU and KNMI that helped and encouraged me. Thank you all for all the lunches, coffee breaks, walks and for the interest we took in each others research. I think we solved most of the problems by explaining to each other what is it that we are doing and why. So many issues can be resolved when we start to really wonder and explain the WHY...

Thank you to all my dear friends from and outside of the university. Thank you for all the encouragement and support, for holding me up when things seemed impossible. Thank you for being around and listening. And above all: thank you to my husband Sander and my daughter Sofia. It's the two of you who made it possible and who kept me motivated, gave me strength and persistence. Thank you for believing in me and making me feel that all is possible. We can do hard things as long as we have each other.